UNIVERSITY OF CRETE
DEPARTMENT OF PHYSICS

Comparison of mass-mapping techniques using weak gravitational lensing.

Application to the UNIONS galaxy survey.

Author:
Andreas Tersenov

Under the supervision of:
Dr. Jean-Luc Starck
&
Prof. Vasiliki Pavlidou

Heraklion, Greece
June, 2023

Abstract

Weak gravitational lensing, the distortion of images of high-redshift galaxies due to foreground matter structures on large scales, is one of the most promising tools of cosmology to probe the dark sector of the Universe. Using the patterns of lensing distortions derived from galaxy shapes, maps of the underlying matter distribution can be obtained. Such maps contain a wealth of information about the distribution of dark matter on large scales, and the origin of the accelerated expansion of the Universe. The aim of this thesis is to study and compare various state-of-the-art map-making methods, namely Kaiser-Squires, Wiener filter, Sparse Recovery and MCALens. In addition, those techniques were applied to the CFIS (Canada-France Imaging Survey) part of the UNIONS (Ultraviolet Near-Infrared Optical Northern Sky) galaxy survey, an ongoing large imaging survey ideally suited for weak lensing. To date CFIS has covered $4\,300\,\mathrm{deg}^2$ in the Northern hemisphere in multiple optical bands from various telescopes in Hawaii. The observed data are an integral part of the imaging survey obtained by the European satellite mission Euclid, to be launched in 2023, and these weak-lensing maps will be valuable for subsequent cosmological analyses. Finally, this work further applies peak counting to one of the generated mass maps and, by comparing with simulations, provides constraints on the cosmological parameters, Ω_m (matter density parameter), A_s (primordial power spectrum), and M_ν (sum of neutrino masses).

Acknowledgments

I would like to express my sincere gratitude to my supervisor, Dr. Jean-Luc Starck, for offering me this project and for his continuous support and guidance over the course of this work. His expertise and encouragement were invaluable to the completion of this thesis. Next, I would like to thank my co-supervisor Prof. Vasiliki Pavlidou, for her encouragement and support throughout my master's program. Lastly, I would like to thank Dr. Lucie Baumont for our fruitful collaboration.

Contents

List of Figures

Introduction

Weak gravitational lensing is a powerful tool in modern cosmology. It is a phenomenon that subtly distorts the images of distant galaxies due to the bending of light by the gravitational effects of intervening matter. It allows us to explore the Universe's dark sector, where it can assist to find the answers to some of the most significant questions in cosmology.

The mechanism underlying weak lensing is deeply rooted in the fundamentals of general relativity. It relies on the simple principle that gravity can bend light, just as it influences physical objects. However, observing and measuring these minute distortions is a task that challenges us with immense technical difficulties and requires innovative methodologies and techniques.

Interpreting these distortions or shears provides a means to estimate the distribution of matter between the observer and the distant galaxies. This indirect probe into the large-scale structure of the Universe can unveil the distribution of dark matter, a significant but elusive component of the Universe. Dark matter cannot be detected directly, as it doesn't interact with light or other electromagnetic radiation, but its gravitational effects can be observed, and weak lensing provides one such observational method.

The Universe's large-scale structure, the distribution of dark matter, and the nature of dark energy are interconnected aspects of a cosmological model. Therefore, insights into one can enrich our understanding of the others, providing us a more comprehensive picture of the Universe. Techniques such as mass mapping and peak counting are part of this investigative process, helping us translate observational data into knowledge about the Universe.

The remainder of the thesis is organized as follows: In Chapter 1, we provide a background on weak lensing, covering light propagation in the Universe, shear and convergence, projected overdensity, the lensing power spectrum, the estimation of shear from galaxies, E- and B-modes, and the relationship between shear and convergence. Chapter 2 delves into various mass mapping methods, their theories, and implementations. It examines the Kaiser-Squires reconstruction, Wiener Filtering, Sparse Recovery techniques, and MCALens in detail. Chapter 3 applies the discussed mapping methods to real data from the UNIONS/CFIS survey. It involves the reconstruction of mass maps using these techniques and the subsequent application of weak lensing peak counts to one of the resulting maps. This analysis allows for cosmological inference, providing constraints on the aforementioned cosmological parameters.

Chapter 1

Weak Lensing Background

This chapter seeks to lay the groundwork for understanding weak gravitational lensing, an important astrophysical phenomenon. We begin by discussing light propagation in the Universe, and how the gravitational field of large-scale structures alters its trajectory, resulting in lensing effects. This sets the stage for the exploration of key quantities in weak lensing: shear and convergence. These quantities encode valuable information about the distribution of matter in the Universe. Following this, we delve into techniques for estimating shear from galaxies, while also introducing E- and B-modes, the two components of this field. Lastly, we discuss the relationship between shear and convergence, creating a solid foundation for the mass mapping methods explored in subsequent chapters.

1.1 Light propagation in the Universe

The propagation of light in the universe is affected by the gravitational influence of massive objects along its path. When light passes near a massive object, its trajectory is deflected, leading to phenomena such as gravitational lensing. In the GR formalism, light propagates along null geodesics in curved spacetime, as described by the geodesic equation

$$\frac{d^2 x^\mu}{d\lambda^2} + \Gamma^\mu_{\alpha\beta} \frac{dx^\alpha}{d\lambda} \frac{dx^\beta}{d\lambda} = 0 \tag{1.1}$$

where λ is the affine parameter along the geodesic, x^μ are the spacetime coordinates, and $\Gamma^\mu_{\alpha\beta}$ are the Christoffel symbols associated with the spacetime metric $g_{\mu\nu}$. The null geodesic condition is given by:

$$g_{\mu\nu} \frac{dx^\mu}{d\lambda} \frac{dx^\nu}{d\lambda} = 0 \tag{1.2}$$

Let us consider two light rays, one being the fiducial ray and the other a nearby, arbitrary ray. Both light rays propagate through the spacetime, experiencing the gravitational effects of mass-energy distribution along their paths. The phenomenon of gravitational lensing can be understood as the change in the physical separation between these two rays as they propagate through the curved spacetime.

Let $x^\mu(\lambda)$ and $x^\mu(\lambda) + \xi^\mu(\lambda)$ be the spacetime coordinates of the fiducial light ray and the nearby ray, respectively. The separation vector $\xi^\mu(\lambda)$ describes the physical distance between the two rays at each point along their paths, and it can be shown to satisfy the *geodesic deviation equation*:

$$\frac{d^2 \xi^\mu}{d\lambda^2} = -R^\mu_{\alpha\beta\nu} \frac{dx^\alpha}{d\lambda} \xi^\beta \frac{dx^\nu}{d\lambda} \tag{1.3}$$

where $R^{\mu}_{\alpha\beta\nu}$ is the Riemann curvature tensor. It is useful to define the *optical tidal matrix* as

$$\mathcal{T}^{\mu}_{\beta} = -R^{\mu}_{\alpha\beta\nu}\frac{dx^{\alpha}}{d\lambda}\frac{dx^{\nu}}{d\lambda} \tag{1.4}$$

It describes the effect of tidal forces on the separation vector ξ^{α} between neighboring geodesics. Using this, the geodesic deviation equation can then be rewritten as

$$\frac{d^2\xi^{\mu}}{d\lambda^2} = \mathcal{T}^{\mu}_{\beta}\,\xi^{\beta} \tag{1.5}$$

illustrating how the optical tidal matrix acts on the separation vector to describe the change in separation between neighboring light rays due to tidal forces.

Adopting the notation of [3] that is more suitable for our purposes, the geodesic that the fiducial light ray follows is denoted by $\gamma^{\mu}_{\mathrm{fid}}(\lambda)$ (we choose the parameter λ so that it arrives to the observer at $\lambda = 0$), and the nearby ray is denoted by $\gamma^{\mu}(\lambda, \boldsymbol{\theta})$, where $\boldsymbol{\theta}$ is a 2-dimensional vector describing the angular separation of the two rays on the sky $\boldsymbol{\theta} = (\theta_1, \theta_2)$. The separation vector $\xi^{\mu}(\lambda, \boldsymbol{\theta})$ is then given by

$$\xi^{\mu}(\lambda, \boldsymbol{\theta}) = \gamma^{\mu}(\lambda, \boldsymbol{\theta}) - \gamma^{\mu}_{\mathrm{fid}}(\lambda) \tag{1.6}$$

We are particularly interested in the perpendicular components of this separation vector, as they describe the distortion of the bundle of light rays. To focus on these components, we project the 4-vector $\xi^{\mu}(\lambda, \boldsymbol{\theta})$ onto a 2D plane tangent to the sphere of observer-visible directions and orthogonal to the light ray. We can then define ξ^1 and ξ^2 as the components of $\xi^{\mu}(\lambda, \boldsymbol{\theta})$ within the orthogonal basis of this plane, creating the vector $\xi(\lambda, \boldsymbol{\theta}) = (\xi^1, \xi^2)$. This vector of course adheres to the geodesic deviation equation, which in this notation takes the form:

$$\frac{d^2\xi(\lambda, \boldsymbol{\theta})}{d\lambda^2} = \mathcal{T}(\lambda)\,\xi(\lambda, \boldsymbol{\theta}) \tag{1.7}$$

In order to express the tidal matrix $\mathcal{T}$ in terms of the matter distribution in the universe, we need to assume a homogeneous universe described by the FLRW metric, which models the isotropic and homogeneous distribution of matter on large scales. In the presence of local density fluctuations on scales much smaller than the Hubble length, the spacetime metric can be expressed as a superposition of the FLRW metric and a comoving Newtonian metric characterizing these local density fluctuations:

$$ds^2 = -\left(1 + \frac{2\Phi}{c^2}\right)c^2 dt^2 + \left(1 - \frac{2\Phi}{c^2}\right)a(t)^2\left(d\chi^2 + f_K(\chi)^2 d\Omega^2\right) \tag{1.8}$$

where Φ is the Newtonian potential, $a(t)$ is the scale factor, $f_K(\chi)$ is the comoving distance function, and $d\Omega^2$ is the metric on the unit sphere.

In the weak field limit, where the gravitational potential Φ is much smaller than the speed of light squared ($|\Phi| \ll c^2$), the tidal matrix can be expressed as a sum of a background contribution term, $\mathcal{T}^{\mathrm{bg}}$, and a clump contribution term, $\mathcal{T}^{\mathrm{cl}}$

$$\mathcal{T}_{ij} = \left(\mathcal{T}^{\mathrm{bg}}\right)_{ij} + \left(\mathcal{T}^{\mathrm{cl}}\right)_{ij} \tag{1.9}$$

The background contribution term, $\mathcal{T}^{\mathrm{bg}}$, arises from the FLRW metric and describes the isotropic and homogeneous expansion of the universe. The clump contribution term, $\mathcal{T}^{\mathrm{cl}}$, is associated with the comoving Newtonian metric and captures the effects of local density fluctuations.

In the weak perturbation limit, we can derive explicit expressions for the background and clump contributions to the tidal matrix. For the background contribution term, $\mathcal{T}^{\mathrm{bg}}$, we find:

$$\left(\mathcal{T}^{\mathrm{bg}}\right)_{ij} = -\frac{4\pi G}{c^2}\rho_0(1+z)^5\delta_{ij} \tag{1.10}$$

where ρ_0 is the present-day mean matter density of the universe, G is the gravitational constant, and z is the redshift. For the clump contribution term, $\mathcal{T}_j^{i(C)}$, we obtain:

$$\left(\mathcal{T}^{\text{cl}}\right)_{ij} = -\frac{(1+z)^2}{c^2}\left(2\partial_i\partial_j\Phi + \delta_{ij}\partial_{ij}^2\Phi\right) \tag{1.11}$$

where Φ is the weak, quasi-static, Newtonian gravitational potential, and $\partial_i = \frac{\partial}{\partial\xi_i}$, and $\partial_{ij}^2 = \frac{\partial^2}{\partial\xi_i\partial\xi_j}$.

It is important to note that the background contribution term is proportional to the identity matrix, leading to a uniform stretching or compression of the light bundle in all directions. In the context of gravitational lensing, this term mainly contributes to the overall redshift of light due to the expansion of the Universe. On the other hand, the clump contribution term contains non-zero off-diagonal terms, which account for the local density fluctuations and their associated gravitational potential. These off-diagonal terms imply that the local inhomogeneities affect the propagation of light bundles in a non-uniform and anisotropic manner. In the context of gravitational lensing, these local inhomogeneities lead to the bending and distortion of light bundles, resulting in the formation of arcs, multiple images, or other lensing phenomena such as magnification and shear, which will be discussed in more detail in the following sections.

If we define the *comoving separation vector* $\boldsymbol{x} = (x_1, x_2) \equiv \xi/a$ and the *comoving transverse gradient* $\nabla_\perp \equiv (\partial/\partial x_1, \partial/\partial x_2)$, and use the expressions (1.10), (1.11) contributions to the tidal matrix, the geodesic deviation equation (1.7) can be written in comoving coordinates χ as:

$$\frac{\mathrm{d}^2\boldsymbol{x}}{\mathrm{d}\chi^2}(\chi) + K\boldsymbol{x}(\chi) = -\frac{2}{c^2}\left(\nabla_\perp\Phi(\boldsymbol{x},\chi) - \nabla_\perp\Phi(0,\chi)\right) \tag{1.12}$$

where K is the spatial curvature of the universe. Together with the boundary conditions

$$\boldsymbol{x}(\chi = 0) = 0 \quad \text{and} \quad \frac{\mathrm{d}\boldsymbol{x}}{\mathrm{d}\chi}(\chi = 0) = \boldsymbol{\theta} \tag{1.13}$$

which arise from the definition of ξ, and therefore $\boldsymbol{x}$, the geodesic deviation equation (1.12) has the solution:

$$\boldsymbol{x}(\chi) = f_K(\chi)\boldsymbol{\theta} - \frac{2}{c^2}\int_0^\chi f_K\left(\chi - \chi'\right)\left[\nabla_\perp\Phi\left(\boldsymbol{x}\left(\chi'\right),\chi'\right) - \nabla_\perp\Phi\left(0,\chi'\right)\right]\mathrm{d}\chi' \tag{1.14}$$

where the potential Φ is integrated along the perturbed light path $\boldsymbol{x}(\chi')$. If we work under the so-called *Born approximation*, i.e. we assume that the perturbation of the light ray is small and the potential on the perturbed light path is approximately the same as the on the unperturbed ray, $f_K(\chi')\boldsymbol{\theta}$, (1.14) becomes:

$$\boldsymbol{x}(\chi) = f_K(\chi)\boldsymbol{\theta} - \frac{2}{c^2}\int_0^\chi f_K\left(\chi - \chi'\right)\left[\nabla_\perp\Phi\left(f_K\left(\chi'\right),\chi'\right) - \nabla_\perp\Phi\left(0,\chi'\right)\right]\mathrm{d}\chi' \tag{1.15}$$

The Born approximation has been shown [8] to be remarkably accurate for any weak lensing survey, including full sky surveys and thus it will be assumed throughout this work.

If we introduce the angular separation vector $\boldsymbol{\beta}(\boldsymbol{\theta},\chi) = \boldsymbol{x}(\chi)/f_K(\chi)$ which is the separation seen by an observer when there is no gravitational lensing along the way, we can derive the *lensing equation* dividing (1.15) by the radial comoving distance f_K:

$$\boldsymbol{\beta} = \boldsymbol{\theta} - \boldsymbol{\alpha}(\boldsymbol{\theta}) \tag{1.16}$$

where $\boldsymbol{\alpha}$ is the *deflection angle* – the difference between the apparent angle $\boldsymbol{\theta}$ and the true angular position of the source $\boldsymbol{\beta}$, given by:

$$\boldsymbol{\alpha}(\boldsymbol{\theta},\chi) = \boldsymbol{\theta} - \boldsymbol{\beta}(\boldsymbol{\theta},\chi) = \frac{2}{c^2}\int_0^\chi \frac{f_K\left(\chi - \chi'\right)}{f_K(\chi)}\left[\nabla_\perp\Phi\left(f_K\left(\chi'\right),\chi'\right) - \nabla_\perp\Phi\left(0,\chi'\right)\right]\mathrm{d}\chi' \tag{1.17}$$

Equation (1.17) is usually the one that we refer to as the *lens equation under the Born approximation*.

1.2   Shear and convergence

In the previous section we derived the lens equation (1.16), and now, in order to to quantify the weak lensing effect in terms of local quantities, we will have to linearize the lens equation. We can do this by expanding the lens equation in a Taylor series around $\boldsymbol{\theta}$ and keeping only the first-order terms. The resulting linear mapping between the lensed (or "image") coordinates $\boldsymbol{\theta}$ and the unlensed (or "source") coordinates $\boldsymbol{\beta}$ is described by the *amplification matrix*, which is defined as the Jacobian of the lens mapping $\mathcal{A} \equiv \partial\boldsymbol{\beta}/\partial\boldsymbol{\theta}$, with elements given explicitly by:

$$
\begin{aligned}
\mathcal{A}_{ij}(\boldsymbol{\theta}, \chi) &= \frac{\partial \beta_i}{\partial \theta_j} = \delta_{ij} - \frac{\partial \alpha_i(\boldsymbol{\theta})}{\partial \theta_j} \\
&= \delta_{ij} - \frac{2}{c^2} \int_0^\chi d\chi' \frac{f_K(\chi - \chi') f_K(\chi')}{f_K(\chi)} \frac{\partial^2}{\partial x_i \partial x_j} \Phi\big(f_K(\chi')\boldsymbol{\theta}, \chi'\big)
\end{aligned}
\tag{1.18}
$$

The second term in (1.17) vanishes as it is independent of $\boldsymbol{\theta}$.

It is now useful to define a new quantity $\psi(\boldsymbol{\theta}, \chi)$, called the *lensing potential*, which is related to the projected gravitational potential Φ by:

$$
\psi(\boldsymbol{\theta}, \chi) = \frac{2}{c^2} \int_0^\chi d\chi' \frac{f_K(\chi - \chi')}{f_K(\chi) f_K(\chi')} \Phi\big(f_K(\chi')\boldsymbol{\theta}, \chi'\big).
\tag{1.19}
$$

This quantity allows us to recast equation (1.18) in terms of derivatives with respect to the angular coordinates $\boldsymbol{\theta}$, which are more convenient to work with:

$$
\mathcal{A}_{ij} = \delta_{ij} - \partial_i \partial_j \psi,
\tag{1.20}
$$

where $\partial_i \equiv \partial/\partial\theta_i$. Moreover, this definition of the lensing potential allows us to write the deflection angle in this weak lensing regime as a gradient,

$$
\boldsymbol{\alpha}(\boldsymbol{\theta}) = \nabla\psi(\boldsymbol{\theta}).,
\tag{1.21}
$$

where $\nabla \equiv (\partial/\partial\theta_1, \partial/\partial\theta_2)$ is the gradient operator in 2D taken in terms of $\boldsymbol{\theta}$.

The above analysis can now provide some more physical insight into those quantities. Since, as we said, the amplification matrix provides a mapping from the lensed to the unlensed coordinates, we can see that the Kronecker delta δ_{ij} in (1.20) represents the identity mapping, which describes the case of no lensing, while the term $\partial_i \partial_j \psi$ is a correction to this identity mapping due to the presence of the lensing potential, and it is a measure of the distortion of the image due to the lensing potential. Therefore, we can say that the lensing potential ψ is a two-dimensional scalar function that captures the cumulative gravitational influence of the intervening mass distribution along the line of sight between the observer and the background sources, and it can be thought of as a weighted projection of the three-dimensional gravitational potential onto the celestial sphere. As such, the lensing potential encapsulates the overall deflection effect on the light rays, providing a description of the trajectory of light rays as they traverse through the gravitational potential wells of the intervening matter.

We can further make our understanding of the amplification matrix $\mathcal{A}$ more intuitive by parametrizing it as

$$
\mathcal{A} = \begin{pmatrix} 1 - \kappa - \gamma_1 & -\gamma_2 \\ -\gamma_2 & 1 - \kappa + \gamma_1 \end{pmatrix},
\tag{1.22}
$$

where (γ_1, γ_2) are the two components of the spin-two field named *shear* $\boldsymbol{\gamma}$ and the scalar field κ named *convergence*.

This way, the convergence is defined as

$$
\kappa = \frac{1}{2}(\partial_1\partial_1 + \partial_2\partial_2)\,\psi = \frac{1}{2}\nabla^2\psi,
\tag{1.23}
$$

and the two shear components

$$\gamma_1 = \frac{1}{2}\left(\partial_1\partial_1 - \partial_2\partial_2\right)\psi, \quad \gamma_2 = \partial_1\partial_2\,\psi. \tag{1.24}$$

Using this parametrization we can split the amplification matrix into a traceless symmetric part and a trace part:

$$\mathcal{A} = \begin{pmatrix} 1-\kappa & 0 \\ 0 & 1-\kappa \end{pmatrix} - \begin{pmatrix} \gamma_1 & \gamma_2 \\ \gamma_2 & -\gamma_1 \end{pmatrix}. \tag{1.25}$$

The trace of the amplification matrix represents the convergence, while the trace-free part represents the shear. This helps us see that the convergence and shear parameters have clear physical meanings: the convergence represents the isotropic scaling (radial stretching or compression) of a lensed image, while the shear describes the anisotropic stretching (tangential distortion) of the image.

This parametrization allows us to relate the properties of the amplification matrix directly to the underlying mass distribution and lensing potential. By decomposing the amplification matrix into the convergence and shear components, we can separately study the effects of mass distribution along the line of sight (convergence) and the orientation-dependent stretching (shear). This separation is useful for analyzing the properties of the lensing system and understanding the different contributions to the observed image distortions. The effects of shear and convergence on a circular source are illustrated in Figure 1.1.
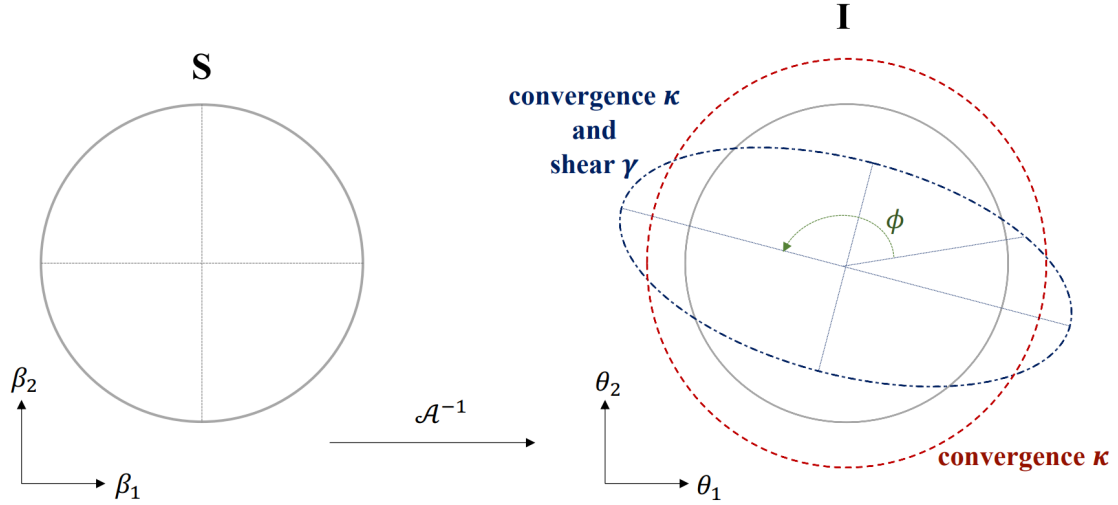
Figure 1.1: Illustration of the effects of convergence and shear on a circular source. The source image is **S** and the lensed image is **I**. The convergence κ causes an isotropic scaling of the image, and its effect is shown in red, while the shear γ causes an anisotropic stretching of the image, and its effect is shown in blue. The norm $|\gamma|$ of the shear determines the flatness of the ellipse and the angle φ determines the orientation of the ellipse. Image taken from [9].

It is convenient to represent the shear as a complex quantity $\gamma = \gamma_1 + i\gamma_2 = |\gamma|\exp(2i\varphi)$, where γ_1 and γ_2 are the two real components of the shear, and φ is the polar angle between the two shear components. This representation of the shear highlights its rotational properties. The lensing effect induces an anisotropic stretching of the image, accompanied by a change in the image's orientation, and the argument of the complex shear, $2\varphi = \arg(\gamma) = \arctan(\gamma_2/\gamma_1)$, describes this change in orientation. The complex shear transforms as a spin-2 quantity, such that a rotation of

the coordinate system by an angle α yields a change in the complex shear by an angle of 2α:

$$\gamma' = \gamma e^{2i\alpha}. \tag{1.26}$$

where γ' represents the transformed shear in the rotated coordinate system. This can also be seen in Figure 1.2, where the shear ellipse is rotated around π.
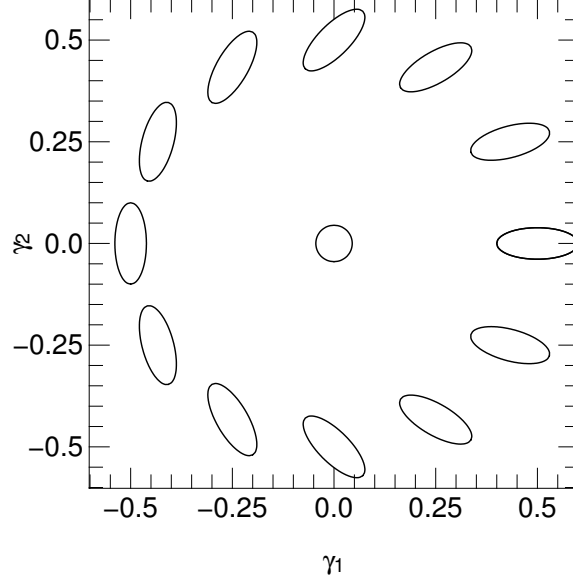
Figure 1.2: Illustration of the shear effect on the circular object at $(\gamma_1, \gamma_2) = (0, 0)$. Each ellipse is a sheared version of this object. The amplitude of $|\gamma|$ of the complex shear remains constant, while the angle φ changes. As φ goes through the range $[0, 2\pi]$, the ellipse is rotated by π. Image taken from [4].

In the context of weak gravitational lensing, the observable quantity of interest is the distortion in the shapes of background galaxies caused by the intervening mass distribution. This distortion is primarily characterized by the shear, γ. However the convergence, κ, which represents the isotropic magnification of the source, also affects the observed galaxy shapes. This makes measuring the shear directly from galaxy images problematic, since both shear and convergence impact the observed image. To account for this effect, we introduce the concept of reduced shear, denoted as g.

The reduced shear, g, is defined as:

$$g = \frac{\gamma}{1 - \kappa}, \tag{1.27}$$

It has the same spin-2 transformation properties as the shear γ, and it represents the actual observable distortion in the shapes of background galaxies, incorporating the combined effects of both shear and convergence. In the weak lensing regime, where both κ and γ are much smaller than 1, the shear γ is a good approximation of the reduced shear g to first order.

1.3 Projected overdensity

The cosmic convergence κ introduced in the previous section bears a significant meaning in the context of cosmological lensing. We have derived this quantity as a direct consequence of the lensing potential ψ and the derivatives thereof. But it is also valuable to study its association with the underlying cosmology, particularly the mass distribution in the universe.

Starting from the expression for the convergence κ as given by

$$\kappa(\boldsymbol{\theta}, \chi) = \frac{1}{2}\nabla^2\psi(\boldsymbol{\theta}, \chi) = \frac{1}{c^2}\int_0^\chi d\chi' \frac{f_K(\chi - \chi')}{f_K(\chi)\,f_K(\chi')}\nabla^2\Phi\left(f_K(\chi')\boldsymbol{\theta}, \chi'\right), \qquad (1.28)$$

we see that it represents the cumulative effect of the lensing potential along the line of sight, where Φ is the gravitational potential, $\boldsymbol{\theta}$ is the position on the sky, and χ is the comoving radial distance. This integral is essentially a projection of the three-dimensional gravitational potential along the line of sight onto the two-dimensional sky. Moreover, we can notice that this equation is actually a 2D Poisson equation, where the gravitational potential Φ is the source term.

We can replace the 2D Laplacian in equation 1.28 with the 3D Laplacian, since it is reasonable to assume that the extra term $\partial^2\Phi/\partial\chi'^2$ vanishes when integrated over the line of sight, as the positive and negative contributions cancel out to a good approximation, under homogeneity arguments. However the Poisson equation is

$$\nabla^2\Phi = 4\pi G\,a^2\,\bar{\rho}\,\delta, \qquad (1.29)$$

where the ∇^2 is the 3D Laplacian, G is the gravitational constant, a is the scale factor, $\bar{\rho}$ is the mean matter density of the universe and δ is the fractional overdensity of matter, defined as

$$\delta(\boldsymbol{x}, \chi) = \frac{\rho(\boldsymbol{x}, \chi) - \bar{\rho}(\chi)}{\bar{\rho}(\chi)}. \qquad (1.30)$$

and so by using equation 1.29 we can rewrite equation 1.28 as

$$\kappa(\boldsymbol{\theta}, \chi) = \frac{4\pi G}{c^2}\int_0^\chi d\chi' \frac{f_K(\chi - \chi')\,f_K(\chi')}{f_K(\chi)}\,a^2(\chi')\,\bar{\rho}(\chi')\,\delta\left(f_K(\chi')\boldsymbol{\theta}, \chi'\right), \qquad (1.31)$$

Now, since as we know from cosmology that $\rho(a) \propto a^{-3}$ and the formula for critical density is $\rho_{c,0} = 3H_0^2/8\pi G$, we can rewrite the above equation as

$$\kappa(\boldsymbol{\theta}, \chi) = \frac{3H_0^2\Omega_m}{2c^2}\int_0^\chi \frac{d\chi'}{a(\chi')}\frac{f_K(\chi - \chi')\,f_K(\chi')}{f_K(\chi)}\,\delta\left(f_K(\chi')\boldsymbol{\theta}, \chi'\right), \qquad (1.32)$$

where Ω_m is the matter density parameter and H_0 is the Hubble constant. This equation shows clearly that the convergence κ is a projection of the matter density along comoving coordinates, weighted by factors depending on the geometry of the universe between the observer and the source. For a universe with flat geometry, the weight function, characterized by $(\chi - \chi')\chi'$, has a parabolic form, peaking at $\chi' = \chi/2$. This indicates that mass distributions located approximately halfway towards the source exert the strongest influence in causing lensing distortions.

We can derive the mean convergence from a multitude of source galaxies by applying the probability distribution of the galaxy sample in comoving distance, $n(\chi)d\chi$, as a weight to the aforementioned expression (the $n(\chi)$ function gives information about how far away the galaxies are from us). This leads to:

$$\kappa(\boldsymbol{\theta}) = \int_0^{\chi_{\text{lim}}} d\chi\,n(\chi)\,\kappa(\boldsymbol{\theta}, \chi) \qquad (1.33)$$

where the integration is performed up to the limiting comoving distance, χ_{lim}, of the galaxy set under consideration. This gives us the expression

$$\kappa(\vec{\theta}) = \frac{3H_0^2\Omega_{\text{m}}}{2c^2}\int_0^{\chi_{\text{lim}}} \frac{d\chi}{a(\chi)}\,q(\chi)f_K(\chi)\,\delta(f_K(\chi)\boldsymbol{\theta}, \chi). \qquad (1.34)$$

where the so-called *lensing efficiency*, q, is defined by:

$$q(\chi) = \int_\chi^{\chi_{\text{lim}}} d\chi'\,n(\chi')\,\frac{f_K(\chi' - \chi)}{f_K(\chi')}, \qquad (1.35)$$

This function represents the cumulative lensing effect at a distance χ due to the distribution of background galaxies. Hence, convergence serves as a linear measure of line of sight projection of the total matter density (for the population of all observed galaxies), taking into account both the geometric attributes of the universe, indicated by distance ratios, and the source galaxy distribution, $n(\chi)\mathrm{d}\chi$.

In practice, for the source galaxy distribution we normally use the redshift distribution of the galaxies, $n(z)\mathrm{d}z$, which is related to the comoving distance distribution by $n(z)\mathrm{d}z = n(\chi)\mathrm{d}\chi$. This distribution is usually derived using *photometric redshifts* or *photo-z*.

Inherently, both shear and convergence have zero expectation values, given that $\langle \delta \rangle = 0$, and hence the first non-zero statistical measure of the κ and γ distribution are their second moments. Also, in the above expressions, the distribution of the source galaxies is assumed to be isotropic, and thus independent of the direction of the line of sight. This in general is a good approximation when far away from galaxy clusters, however in their vicinity this is no longer true, due to the proximity between source galaxies, or between them and the lenses [11, 10, 12].

1.4   The lensing power spectrum

The expression (1.34) shows us the relation between the convergence and the matter overdensity field. The first non-trivial statistical measure of the convergence is the two-point correlation function (2PCF) $\langle \kappa(\boldsymbol{\theta}')\kappa(\boldsymbol{\theta}' + \boldsymbol{\theta}) \rangle$, where $\boldsymbol{\theta}'$ and $\boldsymbol{\theta}' + \boldsymbol{\theta}$ are two points on the sky separated by an angle $\boldsymbol{\theta}$ and $\langle \cdot \rangle$ denotes the average over all angular positions $\boldsymbol{\theta}'$. If we, following the cosmological principle, assume that the density field δ in (1.34) is homogeneous and isotropic on large scales, the convergence field κ will also be homogeneous and isotropic. This means that the 2PCF will only depend on the separation $\boldsymbol{\theta}$ between the two points, and not on their absolute positions. The convergence 2PCF is related to the *convergence power spectrum* $P_\kappa(\boldsymbol{\ell})$ by a Fourier transform:

$$\langle \tilde{\kappa}(\boldsymbol{\ell})\tilde{\kappa}^*(\boldsymbol{\ell}') \rangle = (2\pi)^2 \delta_D(\boldsymbol{\ell} - \boldsymbol{\ell}')P_\kappa(\ell), \tag{1.36}$$

where δ_D is the Dirac delta function and $\tilde{\kappa}(\boldsymbol{\ell})$ is the Fourier transform of $\kappa(\boldsymbol{\theta})$:

$$\tilde{\kappa}(\boldsymbol{\ell}) = \int \mathrm{d}^2\boldsymbol{\theta}\, \kappa(\boldsymbol{\theta})\, \mathrm{e}^{i\boldsymbol{\ell}\cdot\boldsymbol{\theta}}, \tag{1.37}$$

with $\boldsymbol{\ell} = (\ell_1, \ell_2)$ being a 2D wave vector, conjugate of $\boldsymbol{\theta}$ and $\ell = |\boldsymbol{\ell}| = \sqrt{\ell_1^2 + \ell_2^2}$. Again, the power spectrum depends only on the modulus of the wave vector $\boldsymbol{\ell}$, and not on its direction, as a consequence of the cosmological principle.

We should note that since we used the Fourier transform to derive the expression (1.36), we implicitly used the so-called *flat-sky approximation* [41], which implies that the sky is locally flat, and lies on a two-dimensional plane. This approximation is valid for small angular scales, so when we are studying small patches on the sky, but not for large angular scales, where the curvature of the sky must be taken into account. In this case, the power spectrum is calculated using spherical harmonics, instead of Fourier transforms.

The convergence power spectrum is a fundamental statistical tool used to analyze the spatial distribution of matter in the universe. It characterizes the amplitude of fluctuations at each spatial frequency, providing crucial information about the large-scale structure of the universe and the cosmological parameters. As we will show is Section 1.7, the shear is related to the convergence by a simple expression in Fourier space,

$$\tilde{\gamma}(\boldsymbol{\ell}) = e^{2i\beta}\tilde{\kappa}(\boldsymbol{\ell}), \tag{1.38}$$

where β is the position angle of the wave vector $\boldsymbol{\ell}$. This means that the shear power spectrum is equal to the convergence power spectrum $P_\gamma(\boldsymbol{\ell}) = P_\kappa(\boldsymbol{\ell})$.

We can calculate an explicit expression for the convergence power spectrum, depending on the matter power spectrum (the power spectrum of the matter overdensity field $P_\delta(\ell)$), by taking the square of Equation (1.34) in Fourier space, and then inserting the result into Equation (1.36). The result is:

$$P_\kappa(\ell) = \left(\frac{3H_0^2\Omega_m}{2c^2}\right) \int_0^{\chi_{\text{lim}}} \mathrm{d}\chi \, \frac{q^2(\chi)}{a^2(\chi)} P_\delta\left(\frac{\ell}{f_K(\chi)}, \chi\right), \tag{1.39}$$

In deriving this expression, besides the flat-sky approximation, it was also assumed that correlations along the line of sight are negligible, so considered only the modes that lie in the plane of the sky were considered (this is called the *Limber approximation*, [38, 39, 40]).Moreover, the small angle approximation was used, so the first order Taylor expansions of the trigonometric functions were implemented, and the absence of galaxy clustering was assumed.

The convergence power spectrum is a fundamental statistical tool used to analyze the spatial distribution of matter in the universe. It characterizes the amplitude of fluctuations at each spatial frequency, providing crucial information about the large-scale structure of the universe and the cosmological parameters. For weak gravitational lensing, the power spectrum is particularly important because it encodes information about both the distribution of matter (dark and visible) and the geometry of the universe.

1.5 Estimating shear from galaxies

The physical quantity that we measure from galaxy observations is the ellipticity ϵ^{obs} of galaxies, which is a combination of the intrinsic ellipticity ϵ^{s} of the source galaxy and the shear. A crucial challenge in weak gravitational lensing studies lies in deciphering the actual cosmic shear signal from those observed ellipticities.

In general, the intrinsic ellipticity can be defined as a function of the parameters of the ellipse:

$$\epsilon^{\text{s}} = \frac{a - b}{a + b} e^{2i\phi}, \tag{1.40}$$

where a and b are the semi-major and semi-minor axes of the galaxy, and ϕ is the angle between the major axis and the x-axis of the image. With this definition, it can be shown (see [13]) that the way shear modifies the intrinsic ellipticity to the observed one is given by:

$$\epsilon^{\text{obs}} = \frac{\epsilon^{\text{s}} + g}{1 + g^*\epsilon^{\text{s}}}, \tag{1.41}$$

for $|g| \leq 1$, where $g^* = g_1 - ig_2$ is the complex conjugate of the reduced shear $g = g_1 + ig_2$.

In the weak lensing regime ($|g| \ll 1$), the shear is small, and thus we can expand the above expression to first order in g, to get:

$$\epsilon^{\text{obs}} \approx \epsilon^{\text{s}} + g \approx \epsilon^{\text{s}} + \gamma. \tag{1.42}$$

However, this equation still contains two unknowns, the intrinsic ellipticity ϵ^{s} and the shear g, and thus we cannot directly infer the shear of a galaxy from its observed ellipticity. Nevertheless, we can still use the above equation to infer shears of a galaxies, by averaging over a large number of galaxies, and assuming that their intrinsic ellipticity is randomly distributed, without any preferred orientation, and thus its average is zero. So, when using galaxy ellipticities from wide studies, we can write $\langle\epsilon^{\text{s}}\rangle \approx 0$, and get

$$\langle\epsilon^{\text{obs}}\rangle \approx g \approx \gamma. \tag{1.43}$$

where we have also assumed that the shear is the same for all of of the galaxies in the region in study (and that there are no systematics in the shape measurement). So, to put it simply, intrinsic

galaxy ellipticities are statistically random, meaning that the ellipticities of a large number of galaxies would average to zero. On the other hand, gravitational shear introduces a small but coherent distortion to the shapes of galaxies, generating patterns in the ellipticities that are not randomly distributed, but rather are correlated over small angular scales. This way, Equation (1.43) allows us to isolate the shear from the observed ellipticities of a large number of galaxies.

The variance of the observed ellipticity is expressed using equation (1.42) as $\sigma^2(\epsilon^{\mathrm{obs}}) = \sigma^2(\epsilon^{\mathrm{s}}) + \sigma^2(\gamma)$, where $\sigma^2(\gamma)$ is the variance of the shear and $\sigma^2(\epsilon^{\mathrm{s}})$ is the variance of the intrinsic ellipticity, often referred to as the *shape noise*. Of the two terms, the shape noise is usually the dominant one, and so this noise determines the number of galaxies, N, needed to be observed in order to obtain a certain level of accuracy in the shear measurement. The accuracy of the shear measurement is usually expressed in terms of the Signal-to-Noise Ratio (SNR), S/N, which is defined in this case as the ratio of the shear times the square root of the number of galaxies, divided by the shape noise, $S/N = \gamma \, N^{1/2}/\sigma(\epsilon^{\mathrm{s}})$. For typical distortions induced by the large scale structure of the order $\gamma \sim 0.03$, and typical shape noise of the order $\sigma(\epsilon) \sim 0.3$, we get $S/N \sim 0.1 \, N^{1/2}$, which means that for a SNR above unity, we need to observe at least $N \sim 100$ galaxies.

1.6   E- and B-modes

The definitions of the convergence and shear fields, in equations (1.23), (1.24) impose conditions on the forms of the two shear components, γ_1 and γ_2. In particular, the convergence field is a scalar field, and its gradient is curl-free, so if we define a vector field $\boldsymbol{u} = \nabla\kappa$, then $\nabla \times \boldsymbol{u} = 0$. This condition can be expressed in terms of the components of $\boldsymbol{u}$ as $\partial_1 u_2 = \partial_2 u_1$, which, using the definition of $\boldsymbol{u}$, can be written as $\partial_1\partial_2\kappa = \partial_2\partial_1\kappa$. Substituting the expressions for κ, γ_1, γ_2 and ψ, one can obtain second-derivative constraints on the components of the shear field.

We therefore would expect that the observed shear field satisfies those conditions. However, in real-life observations, the vector field $\boldsymbol{u}$ isn't purely a gradient field and does contain a non-zero curl component. This provides a natural way to decompose the shear field into two components, the *E-mode* and *B-mode*, analogous to the polarization states of an electromagnetic field. The E-mode is the component of the shear field that satisfies those conditions, while the B-mode is the component that does not. Similarly, the corresponding convergence field can be decomposed into E- and B-mode components, $\kappa^{\mathrm{E}}, \kappa^{\mathrm{B}}$, which are given by $\nabla^2\kappa^{\mathrm{E}} = \nabla\boldsymbol{u}$ and $\nabla^2\kappa^{\mathrm{B}} = \nabla \times \boldsymbol{u}$.

However, in practice, several factors can contribute to a non-zero B-mode signal. Some of these are associated with systematic errors in the observations or the data analysis pipeline. Examples of potential sources of such systematics include inaccurate PSF correction, misalignment of the telescope, or errors in the shape measurement process. Since these systematics can mimic a curl-like pattern in the shear field, they can generate a spurious B-mode signal.

There are also physical processes that can induce a B-mode component. These include post-Born corrections (higher-order lensing effects), lens-lens coupling, intrinsic alignments of galaxies, and gravitational lensing around massive objects like galaxy clusters where the weak lensing approximation may not hold.

There are several potential sources of the B-mode component. Some of these are associated with systematic errors in the observations or the data analysis pipeline. Examples of potential sources of such systematics include inaccurate PSF correction, misalignment of the telescope, biases in selecting lens galaxies, or errors in the shape measurement process. Since these systematics can mimic a curl-like pattern in the shear field, they can generate a spurious B-mode signal. There are also physical processes that can induce a B-mode component. These include post-Born corrections (higher-order lensing effects in (1.15), or in equations like (1.27)), lens-lens coupling, intrinsic alignments of galaxies (the effect of intrinsic galaxy ellipticities not being randomly distributed, but rather have a preferred orientation), and gravitational lensing around massive objects

like galaxy clusters where the weak lensing approximation may not hold.

The amplitude of the B-mode is usually significantly smaller compared to the E-mode, typically found to be at the percent level relative to the E-mode. To this day, cosmic shear surveys lack the statistical precision to detect these B-modes reliably, and so far B-mode detections have been used primarily for data quality assessment, under the presumption that image and data analysis errors are the only significant B-mode contributor.

1.7 Relation between shear and convergence

So far, we have demonstrated how we can estimate shear from observing galaxy ellipticities. However, sometimes it is more convenient to work with the convergence field. As we have mentioned, the convergence has the effect of isotropically magnifying the image of a source galaxy, and so one way to estimate the convergence is to directly measure the magnification of the source galaxy images. This method however has a lot of challenges, and it is out of the scope of this thesis. Instead, we will focus on a different, indirect method of estimating the convergence, by reconstructing it from the shear field.

The definitions of the convergence and shear fields through the lensing potential, as shown in (1.23), (1.24) show that those two quantities are not independent. If we Fourier transform these two expressions, we get:

$$\tilde{\kappa}(\boldsymbol{k}) = \frac{k_1^2 + k_2^2}{2}\,\tilde{\psi}(\boldsymbol{k}), \tag{1.44}$$

$$\tilde{\gamma}_1(\boldsymbol{k}) = \frac{k_1^2 - k_2^2}{2}\,\tilde{\psi}(\boldsymbol{k}), \quad \tilde{\gamma}_2(\boldsymbol{k}) = k_1 k_2\,\tilde{\psi}(\boldsymbol{k}). \tag{1.45}$$

where $\tilde{\kappa}$, $\tilde{\gamma}_1$, $\tilde{\gamma}_2$ are the Fourier transforms of the convergence and shear components, respectively, and $\tilde{\psi}$ is the Fourier transform of the lensing potential. Also, the 2D wave vector $\boldsymbol{k} = (k_1, k_2)$ is the Fourier dual of $\boldsymbol{\theta}$. From these we see directly that

$$\tilde{\gamma}(\boldsymbol{k}) = \tilde{\gamma}_1 + i\tilde{\gamma}_2 = \frac{k_1^2 - k_2^2 + 2ik_1 k_2}{2}\,\tilde{\psi}(\boldsymbol{k}) = \frac{(k_1 + ik_2)^2}{2}\,\tilde{\psi}(\boldsymbol{k}), \tag{1.46}$$

and thus

$$\tilde{\gamma}(\boldsymbol{k}) = \frac{(k_1 + ik_2)^2}{k^2}\,\tilde{\kappa}(\boldsymbol{k}) = e^{2i\beta}\,\tilde{\kappa}(\boldsymbol{k}), \tag{1.47}$$

where $k = \sqrt{k_1^2 + k_2^2}$ and $\beta = \arctan(k_2/k_1)$ is the polar angle of the complex $\boldsymbol{k}$.

Inverting this relation, we get

$$\tilde{\kappa}(\boldsymbol{k}) = \frac{\left(k_1^2 - k_2^2\right)}{k^2}\,\tilde{\gamma}_1(\boldsymbol{k}) + \frac{2k_1 k_2}{k^2}\,\tilde{\gamma}_2(\boldsymbol{k}). \tag{1.48}$$

This estimator of convergence was first proposed be Kaiser and Squires [14] and is called the *Kaiser-Squires* (KS) estimator. It is important to note that this expression is undefined for $k_1 = k_2 = 0$, which is the zero mode of the Fourier transform, and thus the estimator cannot be used to recover a constant convergence field, meaning that we can only recover the convergence up to a constant. This is called the *mass sheet degeneracy*. The equivalent expression for the estimator (1.48) in real space is given by the integral:

$$\kappa(\boldsymbol{\theta}) = \frac{1}{\pi}\int_{\mathbb{R}^2} \mathrm{d}^2\boldsymbol{\theta}'\,\mathcal{D}^*(\boldsymbol{\theta} - \boldsymbol{\theta}')\,\boldsymbol{\gamma}(\boldsymbol{\theta}') + \kappa_0, \tag{1.49}$$

where the convolution kernel $\mathcal{D}$ is just π times the Fourier transform of the KS estimator in (1.48) and $\mathcal{D}^*$ is its complex conjugate. The extra κ_0 is an arbitrary constant (due to the mass sheet

degeneracy). This way, the convergence can be estimated by convolving the shear field with the kernel $\mathcal{D}$, which means that the relation between the two is linear.

There are however a few issues that make the application of this simple formula on the shear to obtain the convergence non-trivial. First, as was mentioned from the beginning by Kaiser and Squires [14], the substitution of the integral in (1.49) with a discrete sum over galaxies results in infinite noise in the convergence field. This happens because the sampled uncorrelated intrinsic ellipticities of galaxies introduce a white spectrum noise and consequently make (1.49) diverge at high frequency. To cure this problem, some form of smoothing is required, which will inevitably lead to a loss of information, i.e. decreased resolution and correlated noise. Moreover, since the integral in (1.49) is over an infinite area, when we apply it to a finite field of view, we need to modify the algorithm in order to account for the boundaries, to avoid edge effects. Also, of course, without any additional information, the mass sheet degeneracy cannot be lifted, and thus the convergence field will only be recovered up to a constant. Finally, the KS estimator is defined in terms of the shear γ, but as we discussed previously, in practice we only have access to the reduced shear g, which is related to the shear by (1.27). When we are well within the weak lensing regime (where we can approximate $g \approx \gamma$), which is the case when we are mapping at large scales, this is not an issue. However, on small scales, e.g. close to galaxy clusters, where the shear is large, this approximation is not valid, we cannot use the reduced shear as a proxy for the shear.

Despite the aforementioned challenges, mass maps derived from weak gravitational lensing data offer several advantages over studying the shear field directly. Firstly, convergence maps are more intuitive and visually insightful compared to shear fields, as they provide a direct and un-ambiguous spatial representation of the matter distribution along the line of sight. This visual representation lends itself well to an intuitive understanding of the large scale structure of the universe, as well as to comparisons with maps of other tracers of the matter distribution, such as galaxy surveys, X-ray maps or the Sunyaev-Zel'dovich effect. Moreover, when studying higher-order correlations, which provide a measure of the statistical properties of a field that go beyond simple two-point correlations (such as power spectra), convergence maps present a more straight-forward and accessible path compared to shear fields. Higher-order correlations encompass information about the non-Gaussian nature of the field, which is especially relevant for weak lensing studies because the nonlinear evolution of cosmic structures and the lensing effect itself intro-duces non-Gaussianities in the cosmic shear and convergence fields. In this context, convergence reconstructions are very helpful, usually providing the κ field directly in the Fourier space, which makes the calculation of higher-order correlations much simpler.

Over the years, a range of other mass mapping methods were developed, based on different approaches, such as sparsity, wavelets, or machine learning. Each of these methods has its own advantages and disadvantages, and the choice of which one to use depends on the specific ap-plication. In the next section of this thesis, we will introduce and analyze in detail some of these methods.

Chapter 2

Mass mapping methods

At the end of the previous section, we showed how the convergence field can be reconstructed from the shear field, with the Kaiser-Squires estimator (1.48). However, as mentioned, this estimator is not the only way to obtain the convergence from the shear, and in fact, there are several other mass mapping methods that have been developed in the field of weak gravitational lensing. In this section, we will introduce and study in detail some of these methods, and we will discuss their advantages and disadvantages. We will start with a more thorough analysis of the Kaiser-Squires estimator, and then we will move on to more sophisticated methods, namely the Wiener filter, the sparsity-based method, and the MCALens.

2.1 Kaiser-Squires reconstruction

The first mass mapping method that we will study is the Kaiser-Squires (hereafter KS), which we already introduced in Section 1.7. Developed by Nick Kaiser and Gwyneth Squires in 1993 [14], and further improved in [25, 26, 13, 27], this method is a direct linear inversion based on smoothing with a fixed kernel (direct deconvolution). The core of the KS reconstruction technique is the estimator (1.48), that we already derived in Section 2.1. Here, we will study this method in more detail, and show how it is implemented in practice.

2.1.1 Theory

As we have already seen, convergence and shear are related by the following equation in Fourier space:

$$\tilde{\gamma}(\boldsymbol{k}) = \frac{(k_1 + ik_2)^2}{k^2}\, \tilde{\kappa}(\boldsymbol{k}) = \frac{k_1^2 - k_2^2 + 2ik_1k_2}{k^2}\, \tilde{\kappa}(\boldsymbol{k}). \tag{2.1}$$

This can be written as the element-wise multiplication

$$\tilde{\gamma}(\boldsymbol{k}) = \frac{1}{\pi}\tilde{\mathcal{D}}(\boldsymbol{k})\tilde{\kappa}(\boldsymbol{k}), \tag{2.2}$$

where $\tilde{\mathcal{D}}(\boldsymbol{k})$ is the Fourier transform of the kernel $\mathcal{D}(\boldsymbol{\theta})$:

$$\mathcal{D}(\boldsymbol{\theta}) = -\frac{1}{(\theta_1 - i\theta_2)^2}, \quad \tilde{\mathcal{D}}(\boldsymbol{k}) = \pi\, \frac{(k_1^2 - k_2^2 + 2ik_1k_2)}{k^2}, \tag{2.3}$$

and of course θ_1, θ_2 are the components of the angular position $\boldsymbol{\theta}$, and k_1, k_2 are the components of the wave vector $\boldsymbol{k}$. Using $\tilde{\mathcal{D}}\tilde{\mathcal{D}}^* = \pi^2$, we can inverse this relation to obtain

$$\tilde{\kappa}(\boldsymbol{k}) = \frac{1}{\pi}\tilde{\gamma}(\boldsymbol{k})\tilde{\mathcal{D}}^*(\boldsymbol{k}), \quad (k \neq 0), \tag{2.4}$$

which is the equivalent of (1.48) in this notation.

The respective real-space expressions are

$$\gamma(\boldsymbol{\theta}) = \frac{1}{\pi}\int_{\mathbb{R}^2} d^2\boldsymbol{\theta}'\, \mathcal{D}(\boldsymbol{\theta} - \boldsymbol{\theta}')\kappa(\boldsymbol{\theta}'), \tag{2.5}$$

and

$$\kappa(\boldsymbol{\theta}) = \frac{1}{\pi}\int_{\mathbb{R}^2} d^2\boldsymbol{\theta}'\, \mathcal{D}^*(\boldsymbol{\theta} - \boldsymbol{\theta}')\gamma(\boldsymbol{\theta}') + \kappa_0. \tag{2.6}$$

with the latter already introduced in section 1.7.

We can also notice that those relations produce a complex convergence field. In fact, the real part of this reconstructed convergence is the E-mode component, while the imaginary part is the B-mode component.

2.1.2 Implementation

For a practical implementation of this analytical method, we need to discretize the integrals in the real-space expressions, and take into account some statistical uncertainties associated with the real-world data. Doing that for Equation (2.5), and adopting matrix notation, we may write for the observed shear field $\boldsymbol{\gamma}$:

$$\boldsymbol{\gamma} = \mathbf{A}\boldsymbol{\kappa} + \mathbf{n}, \tag{2.7}$$

where $\mathbf{A}$ is the convolution matrix (we may say that it is the discrete version of equation (2.5), so it corresponds to the linear transformation from ideal κ-field to ideal γ-field), $\boldsymbol{\kappa}$ is the underlying convergence field, and $\mathbf{n}$ is the noise vector due to the shape noise (see Section 1.5), whose elements can either correspond to the individual shear measurements or to measurements binned into angular pixels (in the latter case, $\mathbf{n}$ is just the average noise in the pixel) [31]. In this way, Equation (2.5) is expressed as a linear model for the vector $\boldsymbol{\gamma}$ whose elements are the complex shear measurements binned into angular pixels in a two-dimensional image format.

The matrix $\mathbf{A}$ can be decomposed in Fourier space as $\mathbf{A} = \mathbf{F}\mathbf{P}\mathbf{F}^*$, where $\mathbf{F}$ is the discrete Fourier transform matrix, and $\mathbf{P}$ is the diagonal matrix that represents the operator $\frac{1}{\pi}\tilde{\mathcal{D}}(\boldsymbol{k})$, i.e. in the absence of noise,

$$\tilde{\boldsymbol{\gamma}} = \mathbf{P}\tilde{\boldsymbol{\kappa}} = \left(\frac{k_1^2 - k_2^2}{k^2} + i\frac{2k_1 k_2}{k^2}\right)\tilde{\boldsymbol{\kappa}}. \tag{2.8}$$

where $\tilde{\boldsymbol{\kappa}} = \mathbf{F}\boldsymbol{\kappa}$ [30].

An important detail is that the KS inversion, when applied in real space, involves computations with matrices $\mathbf{A}$ and $\mathbf{A}^\dagger$ that are not diagonal, due to the discretization of the smooth shear into a bounded region making the property $\mathbf{A}\mathbf{A}^\dagger = \mathbf{I}$ not exact. This would result into the inversion requiring a greater computational time, and that is why the KS reconstruction is normally implemented within Fourier space, where those matrices are diagonal.

As already mentioned at the end of Section 1.7, one of the caveats of this method is that the generated shear is notably smaller than the noise associated with galaxy shapes, and there exist regions in the sky devoid of galaxies usable for our purposes. These factors, namely the noise from galaxy shapes and the irregular distribution of background galaxies, introduce uncertainties in this otherwise noisy reconstruction process. A potential solution to reduce shape noise per pixel

and avoid vacant pixels is to aggregate the shear measurements into larger pixels. However, this approach compromises the information at smaller scales and is unable to address issues related to survey masks or borders.

What is typically done to reduce the noise is to apply a smoothing filter to the reconstructed convergence map. This act of smoothing however has its trade-offs as well. While it does successfully dampen noise, it also has the potential to blur out or diminish structures on smaller scales, and suppress the peaks in the convergence. Most commonly, smoothing is done by convolving the map with a Gaussian kernel, whose standard deviation σ_{smooth} is a free parameter that can be chosen. This parameter essentially dictates the extent of smoothing – a larger σ_{smooth} results in more smoothing, and conversely, a smaller σ_{smooth} results in less.

The choice of the Gaussian kernel is popular for several reasons. Generally, the Gaussian function has the unique property of being separable, which means that a 2D Gaussian can be written as a product of two 1D Gaussians. This drastically simplifies the convolution operation, particularly for higher-dimensional data. Moreover, the Gaussian function assigns higher weights to the points closer to the center of the kernel and less weight to the points farther away, which allows it to preserve the local features of the image while smoothing out noise, while also ensuring that the boundaries of structures are not significantly distorted during the smoothing process. Finally, the Fourier transform of a Gaussian function is also a Gaussian, which simplifies the analysis in the frequency domain.

Despite its limitations, the KS method of mass reconstruction has proven itself to be a very useful tool in weak lensing cosmology. One of its most appealing attributes is the straightforwardness of its implementation; the method is not only easy to understand but also computationally inexpensive, making it accessible to a wide variety of applications. Furthermore, the Kaiser-Squires method is also local, implying that the estimated convergence at a point only depends on the shear at that point and its immediate neighbours, making it less prone to large-scale systematic effects. Importantly, this method doesn't require any assumptions about the underlying mass distribution, offering an unbiased lensing potential when the Born approximation holds.

2.2   Wiener Filtering

The Wiener filter, named after the American mathematician Norbert Wiener, who introduced it in 1949 [42], is a method of estimating a signal from noisy data. It is a linear filter that minimizes the mean squared error between the estimated and the true signal, given prior knowledge of the signal and noise statistics. In the context of weak lensing, the Wiener filter can provide a statistically optimal reconstruction of the convergence field.

So let us see in detail how the Wiener filter works in our case. We start with the expression of the mass mapping problem in the form of the linear problem in Equation (2.7), assuming that the noise $\mathbf{n}$ uncorrelated. Then, the Wiener filter reconstruction of the convergence field is given by the linear equation

$$\boldsymbol{\kappa}_W = \mathbf{W}\boldsymbol{\gamma}, \tag{2.9}$$

where $\mathbf{W}$ is the Wiener filter matrix, given by

$$\mathbf{W} = \mathbf{S}_\kappa \mathbf{A}^\dagger \left[\mathbf{A}\mathbf{S}_\kappa \mathbf{A}^\dagger + \mathbf{N} \right]^{-1}. \tag{2.10}$$

Here, $\mathbf{S}_\kappa$ and $\mathbf{N}$ are respectively the covariance matrices of the convergence and the noise, which are predefined in this problem, and given by $\mathbf{S}_\kappa = \langle \boldsymbol{\kappa}\boldsymbol{\kappa}^\dagger \rangle$ and $\mathbf{N} = \langle \mathbf{n}\mathbf{n}^\dagger \rangle$. The covariance matrix $\mathbf{S}_\kappa$ encapsulates our prior knowledge about the convergence field's statistical structure, indicating how elements in the field co-vary, while the noise covariance matrix $\mathbf{N}$ describes the statistical structure of the noise. Assumed to be uncorrelated, $\mathbf{N}$'s diagonal elements represent the variance of the noise in each measurement, reflecting the precision of our measurements.

The Wiener filter provides a linear minimum variance solution, meaning that the Wiener filter matrix $\mathbf{W}$ reduces the variance of the error between the true convergence field and the reconstructed one to a minimum. This error variance is quantified as:

$$\langle (\boldsymbol{\kappa} - \boldsymbol{\kappa}_W)^\dagger (\boldsymbol{\kappa} - \boldsymbol{\kappa}_W) \rangle. \tag{2.11}$$

which from Equation (2.9) is given by

$$\langle (\boldsymbol{\kappa} - \mathbf{W}\boldsymbol{\gamma})^\dagger (\boldsymbol{\kappa} - \mathbf{W}\boldsymbol{\gamma}) \rangle \tag{2.12}$$

This variance term essentially quantifies the average squared difference between our estimated convergence field, $\boldsymbol{\kappa}_W$, and the true convergence field, $\boldsymbol{\kappa}$, providing a measure of how far off our estimates can be, on average, from the true values. This error encapsulates both the bias, which is systematic discrepancies between our estimated and true convergence fields, and the scatter, which represents the random fluctuations around this bias. As such, the variance serves as a fundamental indicator of the accuracy of our estimates. By minimizing this variance (given the statistical properties of the signal and the noise), the Wiener filter optimizes the balance between reducing noise (improving precision) and minimizing bias (improving accuracy), thus providing the best possible estimate of the convergence field.

A different way of looking at the Wiener filter is from the Bayesian perspective. In this view, the mass-mapping problem is treated as a statistical inference problem, where the goal is to infer the most probable value of the convergence field given the observed shear data. In other words, we are seeking to compute the posterior probability distribution of the convergence field, which is given by Bayes' theorem as

$$p(\kappa|\gamma) = \frac{p(\gamma|\kappa)p(\kappa)}{p(\gamma)}. \tag{2.13}$$

Here, $p(\kappa|\gamma)$ is the posterior probability distribution of the convergence field given the shear data, $p(\gamma|\kappa)$ is the likelihood function, which is the probability of observing the shear data given the true convergence field, $p(\kappa)$ is the prior probability distribution of the convergence field (which encodes our precedent knowledge of the convergence field, before observing any data), and $p(\gamma)$ is the evidence, which is the probability of observing the shear data.

For the Wiener filter, we assume that the prior probability distribution of the convergence field is Gaussian, with zero mean and covariance matrix $\mathbf{S}_\kappa$

$$p(\boldsymbol{\kappa}) = p(\boldsymbol{\kappa}|\mathbf{S}_\kappa) = \frac{1}{\sqrt{2\pi \, \det \mathbf{S}_\kappa}} \exp\left[-\frac{1}{2} \boldsymbol{\kappa}^\dagger \mathbf{S}_\kappa^{-1} \boldsymbol{\kappa} \right]. \tag{2.14}$$

which represents the belief that the realization of κ is a realization of a Gaussian random field $\kappa \sim \mathcal{N}(0, \mathbf{S}_\kappa)$. Moreover, we assume that the noise in the shear measurements is uncorrelated and also Gaussian $\sim \mathcal{N}(0, \mathbf{N})$, which means that the likelihood function, sharing the noise properties, will also be Gaussian

$$p(\boldsymbol{\gamma}|\boldsymbol{\kappa}) = \frac{1}{\sqrt{2\pi \, \det \mathbf{N}}} \exp\left[-\frac{1}{2} (\boldsymbol{\gamma} - \mathbf{A}\boldsymbol{\kappa})^\dagger \mathbf{N}^{-1} (\boldsymbol{\gamma} - \mathbf{A}\boldsymbol{\kappa}) \right]. \tag{2.15}$$

where it is assumed that the covariance matrix of the noise $\mathbf{N}$ is known. Having the expressions for the prior and the likelihood, (2.14), (2.15), we can now apply Bayes' theorem (2.13) to compute the posterior probability distribution of the convergence field, which is given by

$$p(\boldsymbol{\kappa}|\boldsymbol{\gamma}, \mathbf{S}_\kappa) \propto \frac{1}{\sqrt{2\pi \, \det \mathbf{S}_\kappa}} \frac{1}{\sqrt{2\pi \, \det \mathbf{N}}} \exp\left[-\frac{1}{2} \boldsymbol{\kappa}^\dagger \mathbf{S}_\kappa^{-1} \boldsymbol{\kappa} - \frac{1}{2} (\boldsymbol{\gamma} - \mathbf{A}\boldsymbol{\kappa})^\dagger \mathbf{N}^{-1} (\boldsymbol{\gamma} - \mathbf{A}\boldsymbol{\kappa}) \right] \tag{2.16}$$

In the above expressions we see quadratic forms of the form $\boldsymbol{\kappa}^\dagger \mathbf{S}_\kappa^{-1} \boldsymbol{\kappa}$ and $(\boldsymbol{\gamma} - \mathbf{A}\boldsymbol{\kappa})^\dagger \mathbf{N}^{-1} (\boldsymbol{\gamma} - \mathbf{A}\boldsymbol{\kappa})$. These forms represent the variances and covariances of the convergence field and the noise, respectively, as weighted by the inverse covariance matrices. These quadratic forms are linked to

the concept of "distance" in the space of the variables under consideration. For instance, the term $(\boldsymbol{\gamma} - \mathbf{A}\boldsymbol{\kappa})^\dagger \mathbf{N}^{-1}(\boldsymbol{\gamma} - \mathbf{A}\boldsymbol{\kappa})$ essentially represents a weighted distance between the data vector $\boldsymbol{\gamma}$ and its estimated version $\mathbf{A}\boldsymbol{\kappa}$, with the weighting given by the inverse noise covariance matrix. This captures how much our estimated signal deviates from the observed data. Similarly, $\boldsymbol{\kappa}^\dagger \mathbf{S}_\kappa^{-1} \boldsymbol{\kappa}$ can be viewed as a measure of the "length" of the vector $\boldsymbol{\kappa}$ in a space where the scale is determined by the covariance matrix $\mathbf{S}_\kappa$.

We now want to find the realization of the convergence field that maximizes the posterior probability distribution 2.16, called the *maximum a posteriori* (MAP) estimate of the convergence field. This value of $\boldsymbol{\kappa}$ would be our best guess of the convergence field, given the observed shear data. In this case, it is convenient to work with the logarithm of the posterior distribution instead, since maximizing the logarithm of the posterior is equivalent to maximizing the posterior itself (the logarithm is a monotonic function). The log-posterior is given by

$$\log p(\boldsymbol{\kappa}|\boldsymbol{\gamma}, \mathbf{S}_\kappa) = -\frac{1}{2}\boldsymbol{\kappa}^\dagger \mathbf{S}_\kappa^{-1}\boldsymbol{\kappa} - \frac{1}{2}(\boldsymbol{\gamma} - \mathbf{A}\boldsymbol{\kappa})^\dagger \mathbf{N}^{-1}(\boldsymbol{\gamma} - \mathbf{A}\boldsymbol{\kappa}) + \text{const.} \tag{2.17}$$

and the MAP estimator is then written as

$$\boldsymbol{\kappa}_{\mathrm{G}} = \arg\max_{\boldsymbol{\kappa}} \left\{ p(\boldsymbol{\kappa}|\boldsymbol{\gamma}, \mathbf{S}_\kappa) \right\} = \arg\max_{\boldsymbol{\kappa}} \left\{ \log p(\boldsymbol{\kappa}|\boldsymbol{\gamma}, \mathbf{S}_\kappa) \right\}$$

$$\propto \arg\min_{\boldsymbol{\kappa}} \left\{ \boldsymbol{\kappa}^\dagger \mathbf{S}_\kappa^{-1}\boldsymbol{\kappa} + (\boldsymbol{\gamma} - \mathbf{A}\boldsymbol{\kappa})^\dagger \mathbf{N}^{-1}(\boldsymbol{\gamma} - \mathbf{A}\boldsymbol{\kappa}) \right\}. \tag{2.18}$$

where the subscript G denotes that we are finding the Gaussian realization of the convergence field. This, using the view of the quadratic forms that we described previously, can be rewritten using the notation for the square of the norm of a vector in a space defined by a covariance matrix Σ, denoted $||\cdot||_\Sigma^2$

$$\boldsymbol{\kappa}_{\mathrm{G}} = \arg\min_{\boldsymbol{\kappa}} \left\{ ||\boldsymbol{\kappa}||_{\mathbf{S}_\kappa^{-1}}^2 + ||\boldsymbol{\gamma} - \mathbf{A}\boldsymbol{\kappa}||_{\mathbf{N}^{-1}}^2 \right\}, \tag{2.19}$$

where $||\cdot||_{\mathbf{S}_\kappa^{-1}}$ and $||\cdot||_{\mathbf{N}^{-1}}$ are the norms induced by the matrices $\mathbf{S}_\kappa^{-1}$ and $\mathbf{N}^{-1}$, respectively. This minimization problem can be easily solved by setting the derivative of the expression inside the curly brackets with respect to $\boldsymbol{\kappa}$ equal to zero, which bears the result that the minimum is achieved at $\boldsymbol{\kappa}_{\mathrm{G}} = \mathbf{W}\boldsymbol{\gamma}$, where $\mathbf{W}$ is exactly the Wiener filter, as we defined it in (2.10). We see therefore that the Wiener filter is the MAP estimator of the convergence field, in the case where the prior and the likelihood are Gaussian.

In general, the assumption of a Gaussian prior is very common in cosmology, relying on on arguments such as the central limit theorem and the principle of maximum entropy. In the case of the convergence field, the assumption of a Gaussian prior is physically motivated for the large scales, where Gaussianity persists from the early Universe. However, on smaller scales, the convergence field is expected to be non-Gaussian, due to the non-linear structure formation, which results in the formation of halos and filaments in the late Universe. Thus, when we deal with small scales, or we make the reconstruction of convergence to infer cosmological parameters from the non-Gaussian component of the density field, and the Wiener filter may not be the optimal mass mapping method.

Also, we should mention that all existing mass mapping methods can be viewed from the Bayesian perspective, as a maximum a posteriori estimator of the convergence field. The difference between the methods lies mostly in the choice of the prior distribution of the convergence field and the specific algorithm implemented for the recovery of a point estimate of the convergence field.

2.2.1 Implementation

The implementation of the Wiener filter requires the evaluation of the matrix $\mathbf{W}$, which contains the covariance matrix of the signal (convergence field) $\mathbf{S}_\kappa$ and the covariance matrix of the noise

N. However, as we see in (2.10), the calculation of **W** requires the inversion of a a combined signal and noise covariance matrix, which as we will see, is not trivial.

Since for this method we assume that the convergence field is a Gaussian random field, its covariance matrix $\mathbf{S}_\kappa = \langle \boldsymbol{\kappa} \boldsymbol{\kappa}^\dagger \rangle$ is diagonal in Fourier space (the different modes are uncorrelated). So we can express the covariance matrix of the convergence field as $\mathbf{S}_\kappa = \mathbf{F}^\dagger \mathbf{C}_\kappa \mathbf{F}$, where **F** is the Fourier transform matrix and $\mathbf{C}_\kappa$ is a diagonal matrix. But, as we know, the elements of the covariance matrix in Fourier space $\mathbf{C}_\kappa$, for a Gaussian random field, are equal to the theoretical power spectrum of the convergence field $P_\kappa(\boldsymbol{\ell})$ (see Section 1.4). This is a very useful property, because the power spectrum of the convergence field is a quantity that can be analytically calculated from cosmological models.

In a perfect world, where the noise is stationary (i.e., it has the same statistical properties at all locations), the noise covariance matrix would be diagonal in Fourier space as well, with diagonal elements equal to the power spectrum of the noise $P_n(\boldsymbol{\ell})$, which would simplify the problem significantly, as the Wiener filter could be implemented straightforwardly in Fourier space with the filter solution given by

$$\tilde{\boldsymbol{\kappa}}_{\mathrm{G}} = \tilde{\mathbf{W}} \tilde{\boldsymbol{\gamma}}, \tag{2.20}$$

with

$$\tilde{\mathbf{W}} = \frac{P_\kappa}{P_\kappa + P_n} \tag{2.21}$$

However, in practice, the noise in this type of data is not stationary. It may depend on the number of shear measurements contributing to each pixel of the shear field, leading to a noise covariance matrix that is diagonal in pixel space, not Fourier space. This is a serious problem, because the signal and noise covariances grow quadratically with the size of the dataset and become too large to be stored and processed as dense matrices. This would be possible to overcome if the signal and noise covariances were structured matrices, e.g. when there are sets of bases where both $\mathbf{S}_\kappa$ and **N** are sparse or diagonal, but as we said, such bases for $\mathbf{S}_\kappa$ and **N** are incompatible.

This incompatibility of bases makes the implementation of the Wiener filter more challenging, as one either has to make an oversimplified assumption that the noise is stationary (which is incorrect), or deal with the computationally expensive and numerically challenging task of inverting a large, dense matrix. To bypass such an inversion of dense matrices, there has been proposed an algorithm [43], where an additional messenger field is introduced, to mediate between the different preferred bases in which signal and noise properties can be specified most conveniently (in this case those are the pixel and Fourier spaces). Using this messenger field, the algorithm iteratively builds up the reconstruction of the signal, converging to the Wiener filter solution. Here however, we will use a slightly different iterative method to circumvent the inversion of the matrices.

The method we will use is based on proximal calculus and is known as Forward-Backward (FB) Proximal Iterative Wiener Filtering, initially proposed by Bobin et al. [44] for Cosmic Microwave Background (CMB) spherical map denoising, and it utilizes the fact that the signal and noise covariance matrices are diagonal in Fourier and pixel space, respectively. To show how this method works, we first have to decompose the Wiener filter optimization problem (2.19) into two separate terms, $f_1(\boldsymbol{\kappa})$ and $f_2(\boldsymbol{\kappa})$, which are both quadratic forms:

$$f_1(\boldsymbol{\kappa}) = \parallel \boldsymbol{\gamma} - \mathbf{A}\boldsymbol{\kappa} \parallel_{\mathbf{N}}^2, \quad f_2(\boldsymbol{\kappa}) = \parallel \boldsymbol{\kappa} \parallel_{\mathbf{S}_\kappa}^2 . \tag{2.22}$$

Aiming to solve this minimization problem, the Forward-Backward method utilizes an iterative fixed point algorithm, employing proximal operators in each step. In simple terms, an iterative fixed point algorithm is a method used to solve problems by repeatedly applying a function until we find a point that does not change under this function. This point, known as the fixed point, often represents an optimal solution to the problem we are trying to solve. The general form of the iterative process is given by:

$$\boldsymbol{\kappa}^{k+1} = \mathrm{prox}_{\mu f_2} \left\{ \boldsymbol{\kappa}_G^k + \boldsymbol{\nabla} f_1(\boldsymbol{\kappa}_G^k) \right\}, \tag{2.23}$$

where the superscript k denotes the iteration number, κ_G^k is the estimate of the convergence field at the k-th iteration, $\nabla f_1(\kappa_G^k)$ is the gradient of the first term of the minimization problem (2.22) at the k-th iteration, and $\mathrm{prox}_{\mu f_2}$ is the proximal operator of the second term of the minimization problem (2.22) at the k-th iteration. In general, the proximal operator of a function f at a point x, denoted as $\mathrm{prox}_{f(x)}$, is defined as the solution to the following minimization problem:

$$\mathrm{prox}_{f(x)} = \arg\min_y \left\{ f(y) + \frac{1}{2} \parallel x - y \parallel^2 \right\}. \tag{2.24}$$

In other words the proximal operator of f at x is the point y that minimizes the sum of $f(y)$ and the squared Euclidean distance between y and x, scaled by $1/2$, and so it provides a way to update x in the direction that most decreases f, while also taking into account the distance from the current point x. In our case,

$$\mathrm{prox}_{\mu f_2} \left\{ \kappa_G^k + \nabla f_1(\kappa_G^k) \right\} = \arg\min_\kappa \left\{ f_2(\kappa) - \left(\kappa_G^k + \nabla f_1(\kappa_G^k) \right) \parallel^2 \right\}. \tag{2.25}$$

The parameter μ is a constant that acts as a step size for the updates. This approach converges when

$$\mu < \frac{2}{\parallel \mathbf{A}^\dagger \mathbf{N}^{-1} \mathbf{A} \parallel_2} \tag{2.26}$$

Here, μ is chosen to be the smallest eigenvalue of the noise covariance matrix $\mu = \min\{\mathbf{N}\}$, so it gives an indication of the smallest variance in the noise across all directions in the data space. This means that the step size is linked to the noise level in the data: the lower the noise, the larger the step size and potentially the faster the convergence.

Each iteration of this Wiener-filtering algorithm consists of a Forward and a Backward step:

1. **Forward step**: This phase involves the computation of an auxiliary variable $\mathbf{t}$ as follows:

$$\mathbf{t} = \kappa^n + 2\mu \mathbf{A}^\dagger \mathbf{N}^{-1}(\gamma - \mathbf{A}\kappa^n), \tag{2.27}$$

   where κ^n is the current estimate for the convergence field. The residual, $(\gamma - \mathbf{A}\kappa^n)$, is calculated by comparing the observed shear field with its prediction based on the current estimate of the convergence field. This residual is back-projected to the convergence field's space via the operation $\mathbf{A}^T \mathbf{N}^{-1}$. The resulting value is then added to the present convergence field estimate, resulting in the auxiliary variable $\mathbf{t}$.

2. **Backward step**: In this phase, the updated estimate of the convergence field is calculated as follows:

$$\kappa^{n+1} = \mathbf{F}^\dagger \left[\mathbf{P}_\kappa \left(\mathbf{P}_\eta + \mathbf{P}_\kappa \right)^{-1} \right] \mathbf{F}\mathbf{t}, \tag{2.28}$$

   Here, $\mathbf{t}$ is transformed into the Fourier space via the Fourier transform operator $\mathbf{F}$. The Fourier coefficients are then multiplied element-wise by the ratio of diagonal matrix formed from the convergence power spectrum $\mathbf{P}_\kappa$ and the sum of $\mathbf{P}_\kappa$ and the matrix $\mathbf{P}_\eta = 2\mu \mathbf{I}$, where $\mathbf{I}$ is the identity matrix. This ratio acts as a frequency-dependent filter. Afterward, the inverse Fourier transform is applied to return to the pixel domain.

The iteration is initiated by setting $\kappa^0 = 0$ and the algorithm iterates between these Forward and Backward steps until a convergence criterion is met. The ratio $\frac{\mathbf{P}_\kappa}{\mathbf{P}_\eta + \mathbf{P}_\kappa}$ is similar to the Fourier domain representation of the Wiener filter (see (2.21)), if the noise were stationary. Here, since the noise is not stationary, $\mathbf{P}_\eta$ is a diagonal matrix with its elements being twice the minimum of the $\mathbf{N}$, thus estimating the "baseline" noise level. We can now see how this algorithm sidesteps any requirement for large-scale matrix inversions. Both $\mathbf{N}$, used in Eq.(2.27), and $\mathbf{P}_\kappa$, used in Eq.(2.28), are diagonal matrices, so we are only using the signal and noise covariance matrices in the Fourier and pixel domains, respectively, where they are diagonal.

Despite its proficiency in recovering the Gaussian component of the convergence field, the standard Wiener filtering approach is sub-optimal in extracting non-Gaussian information from the data. As a result, structures such as peak-like formations in the convergence field might be suppressed. This has led to the development of alternative methods based on sparse recovery techniques.

2.3   Sparse recovery techniques

2.3.1   Theory

Signal decomposition is a fundamental practice in signal processing where a signal is represented or transformed into another domain, known as a "dictionary" (which we will denote here as $\mathbf{\Phi}$). Such a representation of a signal $\mathbf{x}$ in a dictionary $\mathbf{\Phi}$ is denoted as α, and is given by the following equation:
$$\mathbf{x} = \mathbf{\Phi}\alpha. \tag{2.29}$$
In this context, we can understand a dictionary as a collection of basis functions that provides an alternative, and often more convenient, representation of the signal. Commonly utilized dictionaries include transformations like Fourier or wavelet transforms.

A *sparse prior* is an assumption we place on our signal, suggesting that the signal's decomposition in the chosen dictionary, α, will contain many zeros, thus making it "sparse". In the world around us, we often encounter sparse signals. Take a cosine function, for example. While this function may appear complex in the time domain, its transformation in the Fourier domain is quite simple, having only two non-zero coefficients that denote the cosine function's frequency.

However, most signals encountered in real-world applications are not strictly sparse when transformed. Instead, these signals are typically "compressible", meaning that while they do not contain many exact zeros, they possess a considerable number of coefficients that are near zero. When these coefficients are ordered by magnitude, their decay pattern tends to be exponential, closely resembling a Laplace distribution. In practical terms, this allows us to simplify these signals by disregarding coefficients close to zero, resulting in a sparse-like representation.

Now, consider the task of solving a typical linear inverse problem, where the equation $\mathbf{y} = \mathbf{A}\mathbf{x} + \mathbf{n}$ describes our situation. In this equation, $\mathbf{y}$ is our observed data, $\mathbf{A}$ is the forward model of our system, $\mathbf{x}$ represents the true underlying signal we aim to recover, and $\mathbf{n}$ is the noise that contaminates our observations.

A common method to estimate the true signal $\mathbf{x}$ is by utilizing an optimization algorithm called LASSO (Least Absolute Shrinkage and Selection Operator). The LASSO problem is expressed as:
$$\arg\min_{\alpha} \parallel \mathbf{y} - \mathbf{A}\mathbf{\Phi}\alpha \parallel_2^2 + \lambda \parallel \alpha \parallel_1 , \tag{2.30}$$
The variable λ in this equation is a regularization parameter (a Lagrange multiplier) that balances between fidelity to the observed data (first term) and promoting sparsity in the solution (second term). The first term, a χ^2 minimization, embodies the fidelity of the reconstruction to the observed data. It measures the discrepancy between the observed data $\mathbf{y}$ and the signal reconstructed from the sparse coefficients, $\mathbf{A}\mathbf{\Phi}\alpha$. This term aims to minimize the squared differences between the observations and the reconstruction, effectively treating them as residuals. However, this simplistic approach assumes uniform or constant noise across all observations.

In many real-world scenarios, as we mentioned in previous sections, the noise is heteroscedastic, i.e. it varies across the data. When dealing with heteroscedastic noise, each residual contributes unequally to the overall sum, and the variance of the noise becomes an important consideration. We can accommodate for this variability by weighting the residuals according to their respective

noise variances, thereby ensuring that residuals with high noise variance (or low reliability) contribute less to the overall sum than those with low noise variance (or high reliability).

As such, we can adjust the χ^2 term to account for this non-uniformity in the noise, transforming it into a weighted sum of squared residuals, with the weight being determined by the noise variance. When the noise variance is incorporated in this way, the parameter λ, which balances fidelity to data and sparsity, can then be interpreted as the signal-to-noise ratio in the transformed domain.

Regarding the regularization term in (2.30), $\parallel \alpha \parallel_1$, it employs the ℓ_1 norm instead of the more common Euclidean (or ℓ_2) norm. The ℓ_1 norm of a vector is simply the sum of the absolute values of its elements:

$$\parallel \alpha \parallel_1 = \sum_i |\alpha_i| . \tag{2.31}$$

The choice of the ℓ_1 norm here is not arbitrary. It is particularly conducive to promoting sparsity in the solution. While the ℓ_2 norm tends to distribute the error equally among all elements of α, leading to many small but non-zero coefficients, the ℓ_1 norm is less forgiving. It forces more coefficients to shrink to zero, thus encouraging a sparser representation of the signal in the dictionary space.

Determining the best value for λ is typically a practical process, conducted through realistic simulations of both the data and the true signal, with the aim of maximizing a chosen success metric. This selection process can be compared to the choice of a theoretical power spectrum for the Wiener filter or the selection of a smoothing scale for the Kaiser-Squires method.

Finally, it is worth noting that sparse recovery methods are inherently non-linear. As such, deriving their properties analytically can be challenging. Furthermore, they are not always formulated within a Bayesian framework, unlike methods such as the Wiener filter, which explicitly maximizes a known analytic posterior, assuming Gaussian noise and signal with known covariances. Yet, this does not prevent us from estimating the uncertainty of the sparse reconstruction. Noise properties of the data can be propagated through techniques like bootstrapping or Monte Carlo simulations to make frequentist estimates of the error associated with the sparse reconstruction.

2.3.2 Implementation: The GLIMPSE algorithm

In mass reconstruction using sparsity, the specific dictionary we adopt should be dictated by the underlying patterns present in the signal we aim to rebuild. The dictionary that is implemented for weak lensing mass map reconstruction is that of the *wavelet transform*. The wavelet transform is a powerful tool that has been used in many applications, including image compression, denoising, and feature extraction. It decomposes a signal into a set of wavelet functions – waveforms of effectively limited duration that have an average value of zero. These functions are localized in both frequency and spatial domains, contrasting Fourier transforms that extend infinitely.

The wavelet functions can be dilated and translated. Scaling a wavelet involves stretching or compressing it, which is analogous to examining the signal at various frequency bands. Translation, on the other hand, allows us to move our 'window' along the signal, capturing the time or spatial localization. Those proverties give multiresolution capabilities, which are key to capture features at different scales and positions in the lensing signal.

In cosmological considerations, the dominant paradigm of cosmic structure evolution anticipates the creation of quasi-spherical clusters of gravitationally bound matter, which we commonly term as *halos*. Such spatial arrangements of matter in halos align well with the profiles of Navarro-Frenk-White or Singular Isotropic Sphere, which exhibit spherical symmetry. To effectively capture such spherical forms, we require a dictionary that is inherently capable of accurately repre-

senting them. A strong candidate for this purpose are the *isotropic undecimated wavelets*, and particularly the *starlet wavelet*, due to their ability to represent structures resembling the convergence of a dark matter halo, which are usually positive and isotropic.

The application of a sparsity prior in the starlet basis in the GLIMPSE algorithm enforces a cosmological model that treats the matter field as a superposition of multiple spherically symmetric dark matter halos. Although this model somewhat simplifies the intricate nature of the universe, it forms a valid approximation within the non-linear domain of the standard structure formation model. Nevertheless, it's important to note that the GLIMPSE sparsity prior might not be entirely effective for larger scales where the density field is expected to adhere to a Gaussian distribution.

The essence of the GLIMPSE algorithm revolves around solving the following optimization problem:

$$\hat{\kappa} = \arg\min_{\kappa} \ \left\| \mathbf{N}^{-\frac{1}{2}} \left[\gamma - \mathbf{T}^{\dagger} \mathbf{P} \mathbf{F} \kappa \right] \right\|_2^2 + \lambda \left\| \omega \mathbf{\Phi}^{\dagger} \kappa \right\|_1 + i_{\mathrm{Im}(\kappa)=0} \ , \tag{2.32}$$

Here, $\mathbf{F}$ stands for the Fourier transformation matrix, $\mathbf{T}$ is the Non-uniform Discrete Fourier Transform[1] (NDFT) matrix, $\mathbf{P}$ is the Fourier-based matrix associated with the Kaiser-Squires methodology (see equation (2.8)), λ is a sparsity regularization parameter, ω is a weighting diagonal matrix, and $\mathbf{\Phi}^{\dagger}$ is the adjoint operator of the wavelet transformation. The final $i_{\mathrm{Im}(\cdot)=0}$, is an identity function which drives the imaginary part of κ to zero, thereby excluding B-modes [31].

Traditionally, to apply the Fourier transform to non-equispaced data, one would first have to bin the data onto a regular grid, which amounts to a form of interpolation and can smooth out or erase small-scale structures. By using the NDFT, this binning step is bypassed, and thus initial term in (2.32) is able to perform Kaiser-Squires-like step without the need for binning the shear data. This way all fine-scale details in the reconstruction are preserved.

Another important feature is that GLIMPSE uses as γ in (2.32) not the shear, but the reduced shear, which makes its reconstructions more precise, especially in the regions where the approximation $\gamma \approx g$ starts to break down. Additionally, GLIMPSE offers an expansion feature that facilitates joint reconstruction involving the reduced shear and *flexion*.

Flexion is a third-order weak gravitational lensing effect, and involves the change in the lensing shear across the image of a galaxy. It causes asymmetric distortions and is a measure of the rate of change of the gravitational field. Including flexion in the reconstruction algorithm can improve the sensitivity to small-scale mass structures, thus further refining the mass maps produced by GLIMPSE.

Fundamentally, the application of a sparsity prior in the starlet space enforces a cosmological model that regards the matter field as a combination of numerous spherically symmetric dark matter halos. Although this doesn't fully capture the true complexity of the universe, it does provide a reasonable approximation for the non-linear regime of the standard model of structure formation. It is this alignment with the nature of cosmic clustering, along with its unique sparsity-enforcing property, that enables GLIMPSE to yield better results in reconstructing smaller-scale non-Gaussian structures than a method like the Wiener filter, which assumes Gaussianity. On the other hand, the Wiener filter is more effective in reconstructing larger-scale structures, where the density field is expected to adhere to a Gaussian distribution.

---

[1] a variant of the Fourier transform adapted to handle data that is not equally spaced

2.4 MCALens

2.4.1 Theory

In Sections 2.2 and 2.3 we discussed two different approaches to the reconstruction of the convergence field from the shear field. The first approach, the Wiener filter, is based on the assumption that the convergence field is a Gaussian random field. This Gaussian model, while effective in reproducing the large-scale characteristics of the convergence map, tends to downplay or even suppress the so-called peak structures — the highest densities regions in the map that hold valuable information about the underlying matter distribution. In contrast, the second model capitalizes on the concept of sparse recovery, treating the convergence map as compressible or "sparse" when represented in the wavelet domain. This sparse model excels at retrieving detailed peak structures but does not fare as well when it comes to capturing the Gaussian-like statistical properties that emerge on larger scales.

Given the complementary nature of these two approaches, it is natural to try to combine them into a single hybrid model that would be able to capture both the large-scale and small-scale features of the convergence field. This was the motivation behind the development of the MCALens algorithm [30], which we will now discuss in detail.

In the context of this method, the convergence field is modeled as the sum of two components: a Gaussian component κ_{G} and a non-Gaussian component κ_{NG}. This can be written as:

$$\boldsymbol{\kappa} = \boldsymbol{\kappa}_{\mathrm{G}} + \boldsymbol{\kappa}_{\mathrm{NG}}. \tag{2.33}$$

The Gaussian component, $\boldsymbol{\kappa}_{\mathrm{G}}$, is assumed to be inherently non-sparse, obeying Gaussian statistics, while the non-Gaussian component, $\boldsymbol{\kappa}_{\mathrm{NG}}$, is assumed to be sparse, or compressible in the wavelet domain.

In order to achieve this, a strategy called Morphological Component Analysis (MCA) is employed. Originally proposed by Starck et al. in [54] and further elaborated in [53], MCA is a method designed to separate two components mixed within a single signal or image, provided these components have distinct morphological properties.

Although in general, the problem of separating two unknowns from one equation is ill-posed, MCA is able to overcome this obstacle by exploiting the morphological differences between the two components. This is achieved by applying different penalty functions, denoted by $\boldsymbol{C}_{\mathrm{G}}$ for the Gaussian component and $\boldsymbol{C}_{\mathrm{NG}}$ for the non-Gaussian component. Thus, the objective becomes minimizing:

$$\min_{\boldsymbol{\kappa}_{\mathrm{G}}, \boldsymbol{\kappa}_{\mathrm{NG}}} \left\{ \|\boldsymbol{\gamma} - \boldsymbol{A}(\boldsymbol{\kappa}_{\mathrm{G}} + \boldsymbol{\kappa}_{\mathrm{NG}})\|_{\boldsymbol{N}}^2 + \boldsymbol{C}_{\mathrm{G}}(\boldsymbol{\kappa}_{\mathrm{G}}) + \boldsymbol{C}_{\mathrm{NG}}(\boldsymbol{\kappa}_{\mathrm{NG}}) \right\}. \tag{2.34}$$

To achieve this minimization, MCA adopts an alternating scheme:

1. First, it estimates $\boldsymbol{\kappa}_{\mathrm{G}}$ by assuming that $\boldsymbol{\kappa}_{\mathrm{NG}}$ is known and minimizes:

$$\min_{\boldsymbol{\kappa}_{\mathrm{G}}} \left\{ \|(\boldsymbol{\gamma} - \boldsymbol{A}\boldsymbol{\kappa}_{\mathrm{NG}}) - \boldsymbol{A}\boldsymbol{\kappa}_{\mathrm{G}}\|_{\boldsymbol{N}}^2 + \boldsymbol{C}_{\mathrm{G}}(\boldsymbol{\kappa}_{\mathrm{G}}) \right\}. \tag{2.35}$$

2. Then, it estimates $\boldsymbol{\kappa}_{\mathrm{NG}}$ by assuming that $\boldsymbol{\kappa}_{\mathrm{G}}$ is known and minimizes:

$$\min_{\boldsymbol{\kappa}_{\mathrm{NG}}} \left\{ \|(\boldsymbol{\gamma} - \boldsymbol{A}\boldsymbol{\kappa}_{\mathrm{G}}) - \boldsymbol{A}\boldsymbol{\kappa}_{\mathrm{NG}}\|^2 \boldsymbol{N} + \boldsymbol{C}_{\mathrm{NG}}(\boldsymbol{\kappa}_{\mathrm{NG}}) \right\}. \tag{2.36}$$

This iterative approach, alternating between estimating the Gaussian and non-Gaussian components, allows us to extract both components, capitalizing on their distinct morphologies to separate them effectively. In the context of weak lensing mass mapping, this method stands to provide a comprehensive and nuanced view of the convergence field.

2.4.2 Implementation

Gaussian component

For the Gaussian component, the method uses the standard Wiener filter approach, i.e. it is assumed that $\boldsymbol{\kappa}_G$ is a Gaussian random field, with noise covariance matrix $\boldsymbol{N}$. This can be expressed as:

$$C_G(\boldsymbol{\kappa}_G) = \|\boldsymbol{\kappa}_G\|_{\boldsymbol{N}}^2 \,. \tag{2.37}$$

and the minimization problem in equation 2.35 can be solved implementing the proximal iterative Wiener filtering, which we described in Section 2.2.1.

Non-Gaussian component

The primary distinctiveness of the Morphological Component Analysis (MCA) method lies in the way it models the non-Gaussian component of the convergence field. Traditional sparse modelling would suggest implementing ℓ_1 or ℓ_0-norm regularization with a wavelet-based dictionary, as it is done in the GLIMPSE algorithm (see Section 2.3.2). However, it has been shown [30] that this approach faces practical challenges, mainly due to the closeness between large-scale wavelet coefficients and low-frequency Fourier components, which complicates the process of distinguishing them.

To mitigate these challenges, an alternative approach has been implemented as well. It involves the estimation of a set of "active" wavelet coefficients, denoted as Ω. This set comprises the scales and positions where wavelet coefficients exceed a certain threshold, which is typically set to be between 3 and 5 times the noise standard deviation, at the respective scale and position.. The detection of these significant wavelet coefficients is achieved by setting $\Omega_{j,x} = 1$ if a wavelet coefficient is detected at scale j and position x. If no significant coefficient is detected, $\Omega_{j,x}$ is set to zero. This approach is mathematically represented as:

$$\Omega_{j,x} = \begin{cases} 1, & \text{if } \left\| (\boldsymbol{\Phi}^\dagger \mathbf{A}^\dagger \boldsymbol{\gamma})_{j,x} \right\| > \lambda \sigma_{j,x} \\ \\ 0, & \text{otherwise} \end{cases} \tag{2.38}$$

This can be interpreted as a mask in the wavelet domain, which is used to separate the large-scale wavelet coefficients from the low-frequency Fourier components. With the wavelet mask Ω estimated, the non-Gaussian component k is then estimated by the minimization scheme:

$$\min_{\boldsymbol{\kappa}_{\mathrm{NG}}} \left\{ \|\Omega \odot \boldsymbol{\Phi}^\dagger \left((\boldsymbol{\gamma} - \mathbf{A}\boldsymbol{\kappa}_{\mathrm{G}}) - A\boldsymbol{\kappa}_{\mathrm{NG}} \right)\|^2 + C_{\mathrm{NG}} \left(\boldsymbol{\kappa}_{\mathrm{NG}}\right) \right\}, \tag{2.39}$$

where $\odot$ denotes the Hadamard product, $\boldsymbol{\Phi}$ is the wavelet matrix (as in the case of the sparse recovery method), and C_{NG} here is $C_{\mathrm{NG}} = i_{\mathbb{R}}(\boldsymbol{\kappa}_{NG})$.

By using the mask Ω, the MCAlens method effectively changes the data fidelity term (which represents the closeness of the obtained solution to the actual data) in the minimization function, creating a deviation from the traditional MCA approach. While this deviation from the standard form might seem unconventional, it brings an important advantage. That is, when Ω is fixed, the algorithm behaves almost linearly, with only nonlinearity being the positivity constraint imposed on the non-Gaussian component $\boldsymbol{\kappa}_{\mathrm{NG}}$. This linearity allows for the straightforward derivation of an approximate error map by simply propagating noise and relaxing this positivity constraint (see [30]).

The reason for the positivity constraint, is that it ensures that the reconstructed peaks in the convergence map are positive, which corresponds well with the physical expectation. In methods

that do not impose this constraint, peaks can be found to be negative as well, if they are located in a region of the sky that is surrounded by a large void. An important thing to note here is that here, since the peaks are captured by the non-Gaussian component, they will be positive by construction in the component κ_{NG}. However, since the positivity constraint is only imposed on this component, and not on the final convergence map $\kappa = \kappa_{\mathrm{G}} + \kappa_{\mathrm{NG}}$, κ can still exhibit negative values at peak locations.

Finally, it's important this approach doesn't encode explicit prior auto-correlation for the non-Gaussian signal, nor prior cross-correlation between the Gaussian and non-Gaussian components. In reality, such correlations do exist, but their explicit inclusion in the prior would complicate the model both theoretically and practically. However, such correlations are implicitly accounted for in the final reconstruction, as they are inherently captured by the data.

Chapter 3

Application to real data

CFIS is a component of the Ultra-violet Near-Infrared Optical Northern Survey (UNIONS) collaboration which aims at collecting photometric data for Euclid in particular.

3.1 CFIS

The Canada-France Imaging Survey (CFIS) is a key component of the broader Ultraviolet Near Infrared Optical Northern Survey (UNIONS), and represents a substantial research effort aimed at addressing fundamental questions in astronomy. These include the properties and behavior of dark matter and dark energy, the evolution of cosmic structures ranging from individual galaxies to vast clusters, and the assembly and development of the Milky Way. A critical requirement for this scientific endeavor is the collection of uniform and comprehensive data across a range of light wavelengths — specifically, the ultraviolet (u-band) and red (r-band) — which must cover expansive portions of the sky.

Since its inception in 2017, CFIS has been successful in covering 4300 square degrees in the northern hemisphere, and the plan is to expand this coverage to ~ 5000 square degrees by 2025. CFIS is uniquely capable of gathering this high-quality data due to its exceptional sensitivity in the u-band and superb imaging capabilities in the r-band at the Canada France Hawaii Telescope (CFHT). These capabilities make it an excellent tool for studying weak lensing.

Beyond its own scientific objectives, CFIS is also playing a crucial role in the Euclid space mission, a European Space Agency project that aims to investigate dark energy and dark matter by mapping the expansion of the universe. CFIS supplies important data that allow for the calculation of photometric redshifts for the Euclid mission. In this regard, the survey parameters for CFIS have been chosen specifically to provide complementary coverage to that of the Euclid mission. The optimal area for the CFIS's r-band survey, which best supplements Euclid, comprises the northern 5000 square degrees of the extragalactic sky.

Moreover, CFIS is designed to work alongside other large-scale imaging projects and spectroscopic surveys like the Sloan Digital Sky Survey (SDSS) and the Dark Energy Spectroscopic Instrument (DESI). To this end, the CFIS survey aims to cover an area as large as the SDSS region. The coverage plan for CFIS-u is extensive, focusing on regions away from the plane of our own galaxy, while the primary science drivers for CFIS-r require data from the SDSS spectroscopy. The chart in Figure 3.1 shows the sky coverage for CFIS relative to some of those key, complementary surveys.

This strategic coverage leads to a galaxy density of 7 galaxies per square arcminute, a figure
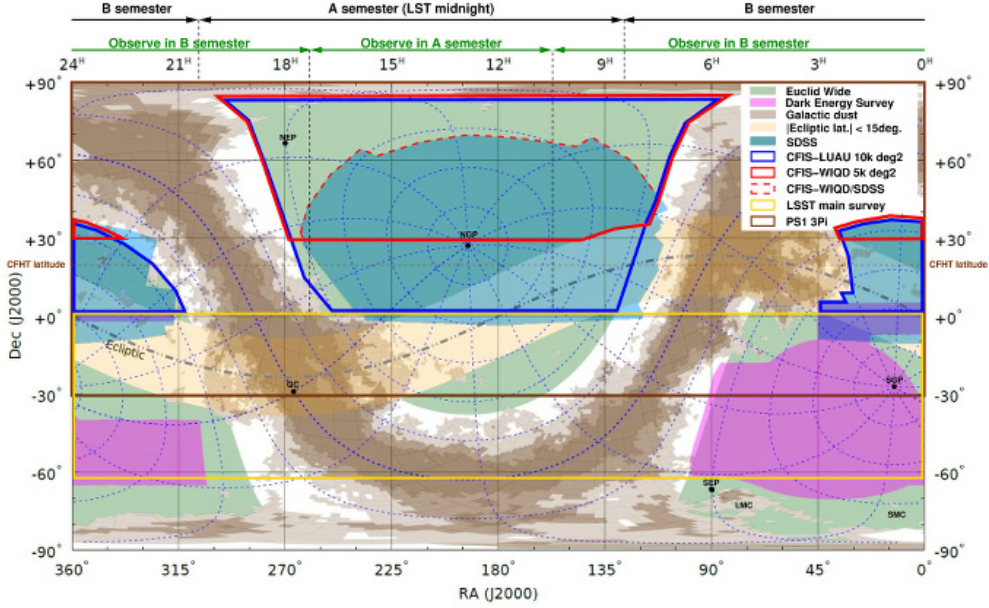
Figure 3.1: Legend: the CFIS-r (red outline) and CFIS-u (blue outline) with respect to other surveys on an equatorial projection of the entire sky. Points of interest are: galactic poles (NGP/SGP), ecliptic poles (NEP/SEP), etc. The CFHT semester boundaries are indicated at the top (based on the LST at midnight) as well as the areas that will be observed from the A and B semesters. This Mercator projection illustrates well the RA pressure of the survey but does not respect the relative areas vs. declination, areas near the equator being larger. For example, the CFIS-u total sky area in blue is double of the CFIS-r outlined in red. Original image credit: T. Dwelly.

similar to that obtained in other surveys like the second Red-sequence Cluster Survey (RCS2), the Kilo-Degree Survey (KiDS), and the Dark Energy Survey (DES). However, CFIS stands out by covering a larger area than RCS2 and KiDS and providing better image quality than DES.

3.2 Data

3.2.1 Catalog

The shear catalog used in this work was built by Guintot et. al [34], from CFIS r-band data (with average seeing of ~ 0.65 arcsec). While the UNIONS survey will be composed of a number of different bands, allowing for the calculation of photometric redshifts for all observed galaxies, at the moment only r-band data has reached a sufficient area and depth. The catalog is composed of $N_{\mathrm{gal}} = 40\,151\,119$ galaxies, and covers an effective area of $A = 1565\,\mathrm{deg}^2$. It is is divided into four patches, referred to as P1 through P4, as shown in Fig. 3.2. The effective density in the catalog is $n_{\mathrm{eff}} = 7.5\,\mathrm{arcmin}^{-2}$, and the corresponding shape noise is $\sigma_{\mathrm{SN}} = 0.28$.

The catalog was derived from an effectively masked area of $A = 1565\,\mathrm{deg}^2$, which includes the shape measurements of $N_{\mathrm{gal}} = 40\,151\,119$ galaxies. The data is divided into four sections, referred to as P1 through P4, as shown in Fig. 3.2. To determine the effective density in the catalog, a formula provided in a previous study [50] was used:

$$n_{\mathrm{eff}} = \frac{1}{A} \frac{\left(\sum_{i=1}^{N_{\mathrm{gal}}} w_i\right)^2}{\sum_{i=1}^{N_{\mathrm{gal}}} w_i^2} \tag{3.1}$$

where w_i is the weight of the i-th galaxy. The corresponding shape noise is derived from:

$$\sigma_{\text{SN}}^2 = \frac{1}{2} \frac{\sum_{i=1}^{N_{\text{gal}}} w_i^2 \left(e_{1,i}^2 + e_{2,i}^2\right)}{\sum_{i=1}^{N_{\text{gal}}} w_i^2} \tag{3.2}$$

where $e_{1,i}$ and $e_{2,i}$ are the components of the ellipticity of the i-th galaxy. The effective density turns out to be $n_{\text{eff}} = 6.76 \, \text{gal} \, \text{arcmin}^{-2}$, and the shape noise is $\sigma_{\text{SN}} = 0.35$. In the later analysis, we focused on the P3 patch, which has an area of $249 \, \text{deg}^2$.
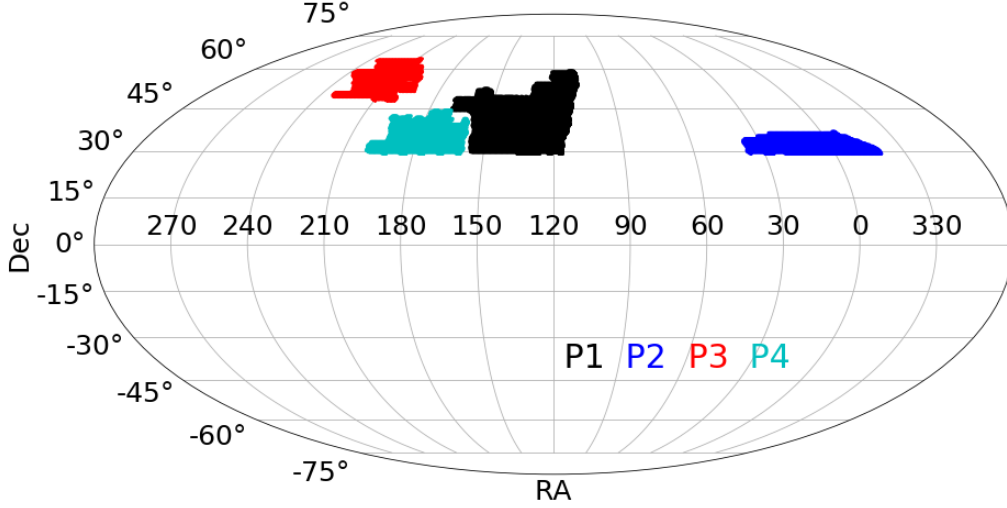
Figure 3.2: The four patches of the CFIS dataset that was used in this work. From left to right: P3, P4, P1 and P2. For the final analysis only the P3 (red) patch, of $249 \, \text{deg}^2$, was employed. Credit [34].

3.2.2 Calibration

The calibration of shears in the catalog was performed using a method called *metacalibration*, first introduced in [51]. This approach calibrates shear measurements, by applying a small shear to the images and measuring the response of the ellipticity. This way, it avoids creating a big number of image simulations (which is done in the traditional calibration approach), which would be computationally expensive.

The way this method works is by calculating the response matrix $\mathbf{R}$ of a shape measurement algorithm, to a small shear g applied to the image. To get this response, we begin by considering the weak lensing equation, used to calculate the mean shear g from the ellipticities of an observed set of galaxies:

$$\langle e_i^{\text{obs}} \rangle = (1 + m_i)\langle g_i \rangle + c_i \tag{3.3}$$

where e_i^{obs} is the i-th component of the observed ellipticity, g_i is the i-th component of the mean shear, m_i is the multiplicative bias, and c_i is the additive bias. The mean shear is calculated from the observed ellipticities, using the weak lensing equation. Here we are assuming that the intrinsic ellipticity of galaxies, on average, nullifies.

This equation can be generalized to relate the observed ellipticity to the shear for a single galaxy of intrinsic ellipticity e_i^{int}:

$$e_i^{\text{obs}} = e_i^{\text{int}} + \sum_{j=1}^{2} \mathbf{R}_{ij} g_j + c_i \tag{3.4}$$

where $\mathbf{R}$ is the response matrix, defined as:

$$\mathbf{R}_{ij} = \frac{\partial e_i^{\text{obs}}}{\partial g_j} \tag{3.5}$$

In order to calculate the response matrix numerically, we need to approximate the derivative in Eq. 3.4, by replacing the derivatives with finite differences. We thus have:

$$\mathbf{R}_{ij} \approx \frac{e_i^{\text{obs},+} - e_i^{\text{obs},-}}{2\Delta g_j} \tag{3.6}$$

where $e_i^{\text{obs},+}$ and $e_i^{\text{obs},-}$ are the observed ellipticities of the galaxy, after applying a small shear $g_j = \pm\Delta g_j$ to the image.

To impose an artificial shear on an image, we first have to remove the influence of its original Point Spread Function (PSF) - this deconvolution and is done through division in the Fourier domain. After deconvolution, an artificial shear is applied, and the image is then reconvolved with a PSF larger than the original. This larger PSF helps smooth out artifacts produced during the deconvolution process, which often arise due to noise in the images.

Next, a noise image (essentially a blank image of the same size as the original but filled with noise) is created with the same variance as the original. This noise image also goes through deconvolution, shearing, and reconvolution. The shearing applied to the noise image is a rotated version, to counteract correlations introduced in the original image due to the shearing process. The modified noise image is then applied to the actual image.

The method results in the creation of five images: four for calibration purposes and one for measurement. The response (correction applied) consists of two parts: the shear response and the selection response. The shear response corrects for the shear bias, including model bias and noise bias. The selection response corrects for biases due to selection effects, like criteria based on brightness or size of objects. To account for these effects, the selection process must be carried out on parameters derived from the sheared images, referred to as the selection mask.

Shear and selection responses can be defined with the following equations:

1. Shear response:

$$\langle \mathbf{R}_{ij}^{\text{shear}} \rangle = \left\langle \frac{g_i^{\text{obs},+,j} - g_i^{\text{obs},-,j}}{2\Delta g} \right\rangle \tag{3.7}$$

where $g_i^{\text{obs},\pm,j}$ is the observed shear of the galaxy image, when it is sheared by $\pm\Delta g$ in the j direction. We take the mean value, because this measurement contains a lot of noise.

2. Selection response:

$$\langle \mathbf{R}_{ij}^{\text{selection}} \rangle = \frac{\langle g_i^{\text{obs}} \rangle_{S^+,j} - \langle g_i^{\text{obs}} \rangle_{S^-,j}}{\Delta g} \tag{3.8}$$

Here, $\langle g_i^{\text{obs}} \rangle_{S^\pm,j}$ is the average ellipticity measured on the image without any applied shear but using the selection mask from the images with a small shear applied. Since the parameters we are selecting are correlated to the shear, different values for this are obtained depending on the sheared image version we apply the cuts to, which results in a nonzero selection response.

The mean response matrix is therefore given by:

$$\langle \mathbf{R}_{ij} \rangle = \langle \mathbf{R}_{ij}^{\text{shear}} \rangle + \langle \mathbf{R}_{ij}^{\text{selection}} \rangle \tag{3.9}$$

This way, we calibrated the shears of the galaxies by applying the inverse of the mean response matrix to the observed ellipticities, according to (3.4).

3.3   Mass Map Reconstruction

Following the detailed description of each method provided in the Section 2, we implemented the described algorithms to produce mass maps from the P3 patch of UNIONS/CFIS data. For the purpose of this study, the `Python` package `cosmostat` which contains a variety of tools for weak lensing mass mapping, was used.

For the methods that require a theoretical power spectrum (namely Wiener filter and MCALens), we used the power spectrum estimated with the public MICE simulated galaxy catalog, constructed from a light cone N-body dark matter simulation [52]. This power spectrum was also used for similar analyses, for data from the DES survey, and since our CFIS data is comparable to DES in terms of depth and resolution, using this power spectrum is a reasonable choice.

3.3.1   Kaiser-Squires

First, to see a picture of our data, we plotted the galaxy number map, shown in Figure 3.3. The map was created by counting the number of galaxies in each pixel of the image with a pixel size of 1.5×1.5 arcmin^2. The resulting map shows the distribution of galaxies in the P3 patch, as well as the masked area.
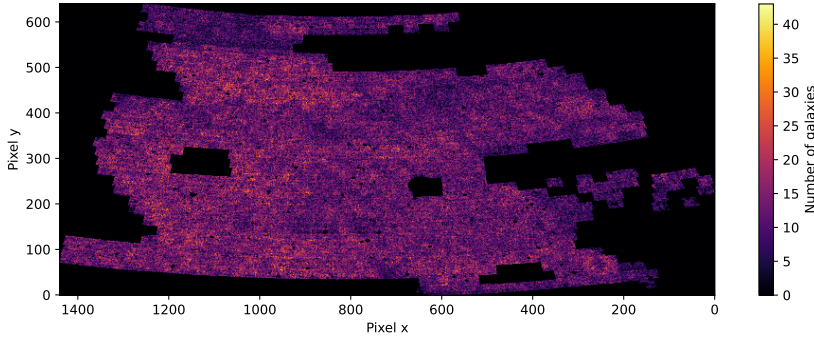

Figure 3.3: Galaxy number map of the P3 patch of the CFIS survey. The masked area is shown in black.

The first method implemented was the standard Kaiser-Squires inversion algorithm. Since this method is not computationally expensive, we were able to run it with higher resolution, using a pixel size of 0.4×0.4 arcmin^2. The resulting mass map (multiplied by the mask) is shown in Figure 3.4. As expected, this map contains a lot of noise. To reduce the noise, we also ran the Kaiser-Squires algorithm with a Gaussian smoothing scale of $\sigma = 2$, which resulted in the mass map shown in Figure 3.5. We can see that the noise is reduced, but the features of the map are also smoothed out. The choice of sigma=2 was based on a compromise between maintaining the features of the mass map and minimizing noise.

For all the other methods, we used a pixel size of 1.5×1.5 arcmin^2, since, because of their higher computational cost, they could not be run on a personal computer with higher resolution.

3.3.2   Wiener Filter

The next method we implemented was the Wiener filter. We used the proximal Wiener filter algorithm, with 100 iterations. The resulting mass map is shown in Figure 3.6. We can see that the
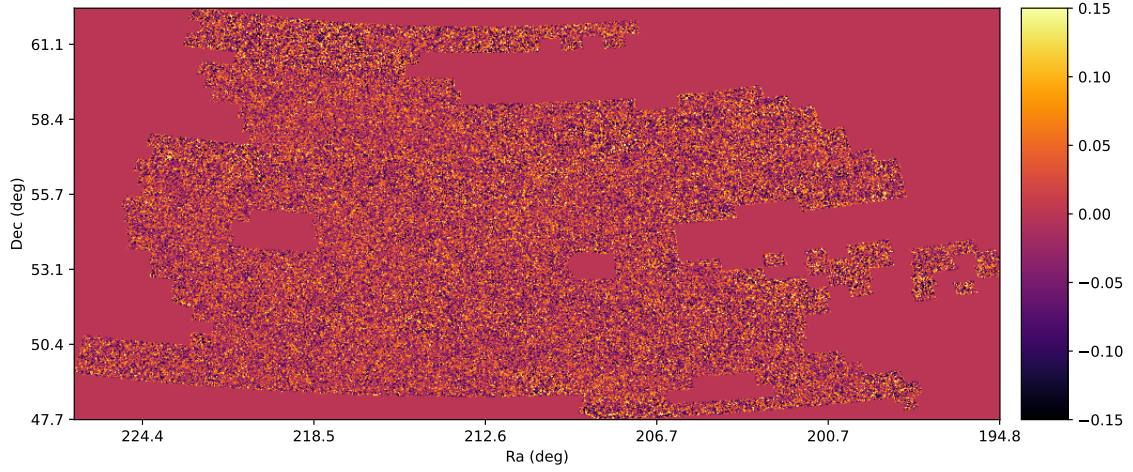
36

Figure 3.4: Mass map reconstructed with the Kaiser-Squires algorithm, with resolution of $0.4 \times 0.4\ \text{arcmin}^2$.

noise is reduced, and the features of the map smoother. We can also observe that the mass map is significantly "weaker" and more diffused compared to KS. This is an expected result, since the Wiener filter is designed to suppress noise, and that comes at the cost of reducing the signal.

The Wiener filter was also implemented with an inpainting feature, designed to handle areas of the data set where information might be incomplete or missing. The choice of inpainting was made in consideration of potential defects in data collection or subsequent processing, which may leave gaps in the data. The resulting mass map is shown in Figure 3.7, in which we also have plotted the contours of the masks with white lines. We can see that the inpainting feature was able to fill in the masked area, and the resulting mass map is very similar to the one without inpainting, in the unmasked region.

When we run a Wiener filtering (or any similar reconstruction method) on a map that contains masked regions, we can end up with peculiar effects at the edges of the data. This is because the reconstruction algorithm doesn't "know" what to do with the masked regions. In the Fourier domain, the mask introduces discontinuities which propagate into the reconstructed map and create spurious correlations, a phenomenon often referred to as "edge effects". While inpainting does generate an estimate of the convergence in the masked regions, it's important to understand that this is not the primary goal of the procedure, especially when the masked regions are large. The data in these regions is essentially unknown, and the inpainting is merely an educated guess based on the surrounding regions. Instead, the main purpose of inpainting in this context is to create a continuous, unmasked map that can be processed by the reconstruction algorithm without introducing edge effects. By filling in the masked regions in a way that is consistent with the observed data, inpainting allows the reconstruction algorithm to operate smoothly across the entire map.

3.3.3 Sparse Recovery/GLIMPSE

The sparse recovery method was applied next, with 20 iterations, and using at first the value $\lambda = 4$ for the regularization parameter. This corresponds to a $\sigma = 4$ detection level on the wavelet coefficients. The resulting mass map is shown in Figure 3.8. We can see that, as was expected it recovers the peaks in the mass distribution, that correspond to the locations of dark matter halos, much better than the other methods. However, on the other hand it does not provide a good estimate of the mass distribution in the regions between the peaks.
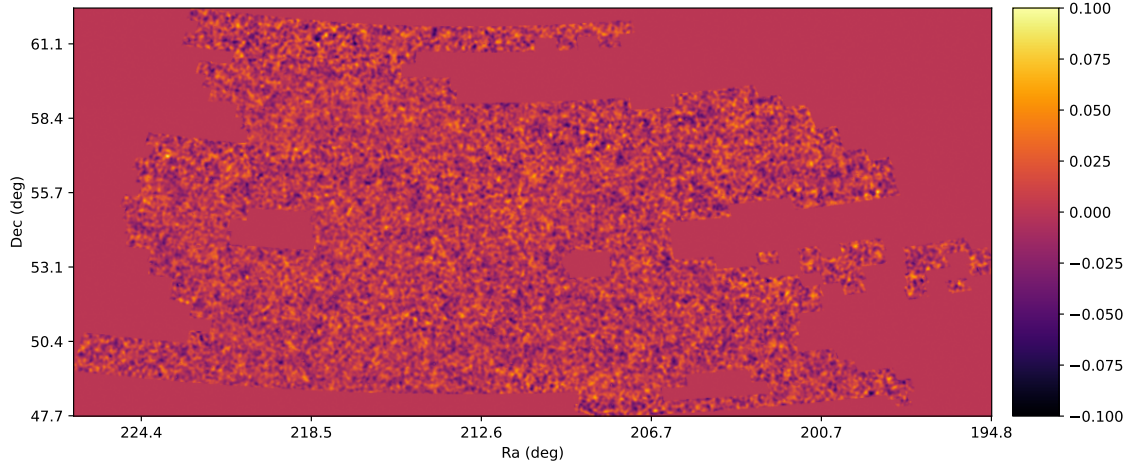
Figure 3.5: Mass map reconstructed with the Kaiser-Squires algorithm, with resolution of $0.4 \times 0.4 \, \mathrm{arcmin}^2$ and Gaussian smoothing scale of $\sigma = 2$.

We also implemented this method with $\lambda = 5$, corresponding to a $\sigma = 5$ detection level on the wavelet coefficients. For the number of iterations we chose again 20, since a larger number of iterations was not possible due to the computational cost The resulting mass map is shown in Figure 3.9. We can see that only the largest peaks are recovered, while the smaller ones are not, since the threshold is set at a higher level.

3.3.4 MCAlens

Finally, the MCAlens technique was implemented using a detection level of the wavelet coefficient at $\sigma = 5$. We used 15 iterations, since again, a larger number of iterations was not possible due to the computational cost. The resulting mass map is shown in Figure 3.10. We can see that the MCAlens method recovers the peaks in the mass distribution well, but it also provides a good estimate of the mass distribution in the regions between the peaks, unlike the sparse recovery method (especially if we compare to the one with the same detection level).

Each of the mass maps resulting from these algorithms was then studied and compared to assess their relative merits. It is important to note that while these maps differ in detail and noise levels due to the different underlying assumptions and methodologies of the techniques, all of them offer valuable perspectives on the mass distribution.

Without a doubt, the most effective methods in capturing peak structures and intricate details in the mass maps were those incorporating sparsity and non-Gaussianity in their models, namely the sparse recovery and MCAlens methods. Despite their increased complexity, these techniques provided a more precise and detailed reconstruction of the mass distribution.

In conclusion, this study showcased the utility and effectiveness of different mass mapping algorithms when applied to the P3 patch of the UNIONS/CFIS data. The results highlight the importance of considering both the nature of the data and the specific aims of the study when choosing the most suitable mass mapping technique. Future studies will aim to refine these methodologies and explore additional techniques in pursuit of even more accurate mass map reconstructions.
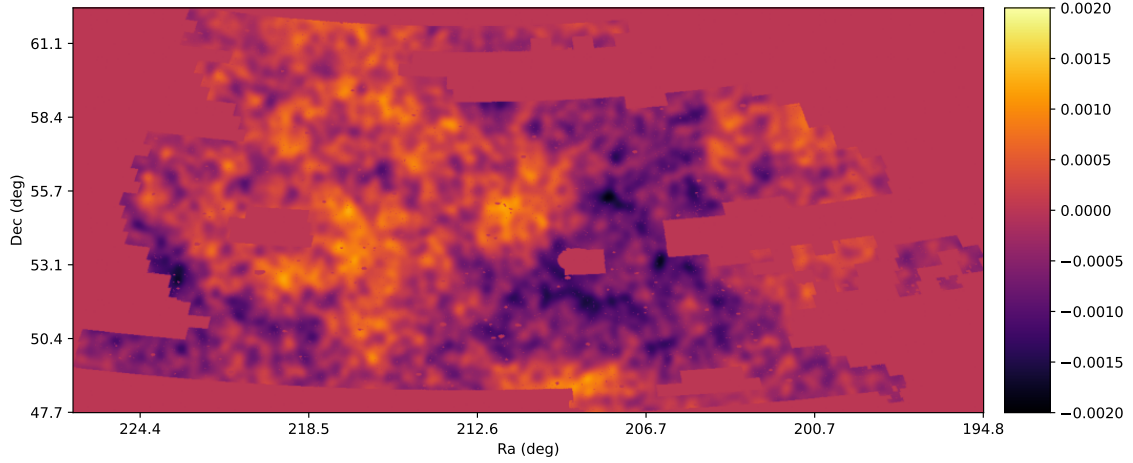
Figure 3.6: Mass map reconstructed with the proximal Wiener filter algorithm with 100 iterations and resolution of 1.5×1.5 arcmin^2.

3.4 Weak Lensing Peak Counts

3.4.1 Weak Lensing Peaks

The traditional statistical methods used in weak lensing mainly focus on second-order statistics, including the two-point correlation function and the power spectrum. These methods are effective at probing the Gaussian properties of the Large Scale Structure. Nevertheless, the non-Gaussian features of the LSS, which arise due to the nonlinear evolution of structures on small scales and low redshifts, can also provide a wealth of cosmological insights. Various higher-order statistics have been proposed to unlock this non-Gaussian information, such as Minkowski functionals, higher-order moments, the bispectrum, and weak lensing peak counts, among others.

In this part of the thesis, we will to study weak lensing peak counts in our recovered mass maps of the P3 patch of the CFIS survey. Peaks in weak-lensing convergence maps are essentially markers of overdense regions. They are defined as local maxima, i.e., a pixel that has a higher value than all of its eight neighbors. The peak function, representing the number of peaks relative to peak height or Signal-to-Noise Ratio (S/N), depends on the nonlinear and non-Gaussian part of the LSS. This higher-order weak-lensing statistic can be employed to constrain cosmological parameters and, when combined with second-order shear statistics, can help remove parameter degeneracies. Moreover, weak lensing peaks offer an indirect way of tracing dark matter halos: large peaks correspond with massive halos, whereas lower-amplitude peaks typically indicate multiple smaller halos along the line of sight. Additionally, lower amplitude peaks can be influenced by mass outside dark matter halos or galaxy shape noise.

To create a complete theoretical prediction of peak counts is a current area, one approach is to generate weak-lensing simulations densely sampled in cosmological parameter space, and use interpolation of these simulations as a surrogate for prediction. These simulations have the advantage of being able to include the exact survey mask and shape noise. Here, we utilize the `MassiveNuS` simulations to predict peak counts (see Section 3.4.3 for more details). By comparing the peak counts of the CFIS P3 patch with the predictions from the `MassiveNuS` simulations, it is possible to obtain constrains for some cosmological parameters. This was done here implementing the inference pipeline `shear-pipe-peaks` [17].
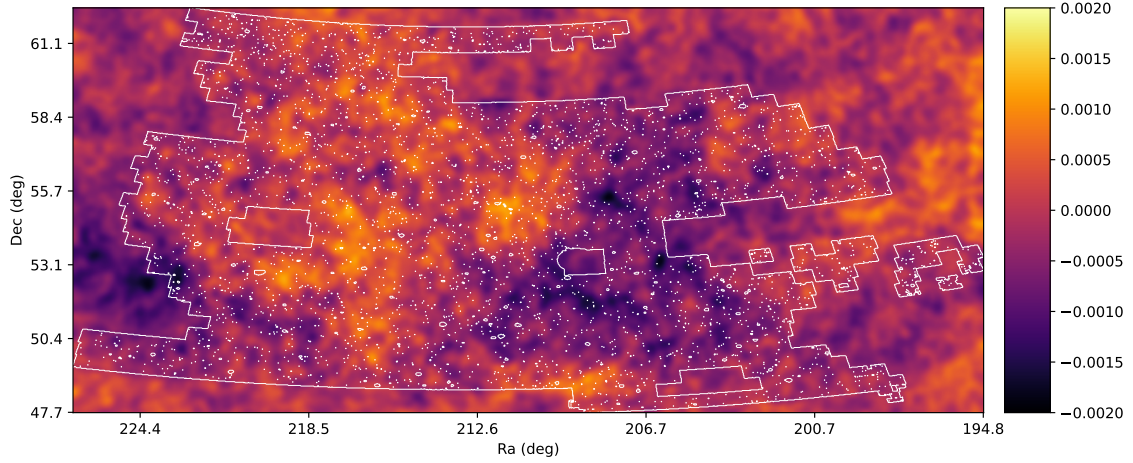
39

Figure 3.7: Mass map reconstructed with the proximal Wiener filter algorithm with 100 iterations and resolution of $1.5 \times 1.5 \, \text{arcmin}^2$, with inpainting.

3.4.2 Counting Peaks in CFIS Mass Maps

For the peak count analysis, we use the mass map of the CFIS P3 patch recovered with the smoothed Kaiser Squires algorithm. This mass map was chosen because it has the resolution of $0.4 \times 0.4 \, \text{arcmin}^2$, which is the required resolution for later comparison with the simulated mass maps. Moreover, in order to match the size of the simulation convergence maps, which are 512×512 pixels, we – following [20], where a similar analysis has been implemented, for an earlier version of the P3 catalog – make 12 cutouts of the CFIS mass map, each of size 512×512 pixels. We choose the cutouts to be non-overlapping and to be away from the edges of the mass map, to avoid including any edge effects. The P3 mass map with the cutouts in black boxes is shown in Figure 3.11.

We then counted the peaks in each of the 12 cutouts. To do this, we first created the respective SNR map for each cutout. The SNR maps here are the noisy convergence maps, smoothed with a Gaussian filter over the standard deviation of the noise. An example of the SNR map for one of the cutouts is shown in Figure 3.12. We identified the peaks as local maxima in the SNR maps, using the `lenspack` package, and afterwards averaged the peak counts over the 12 cutouts. The histogram that we obtained is shown in Figure 3.13. For the histogram of each cutout we considered 30 bins, spaced evenly in the range $\text{SNR} = [-2, 6]$.

3.4.3 Simulations

In order to generate estimates for the statistical parameters used for inferring cosmological parameters, we utilized the `MassiveNuS` simulation suite. This is a suite of cosmological N-body simulations, which consist solely of dark matter and encompass a range of cosmological models, including massive neutrinos with mass sum from 0 to 0.62 eV. The box size of these simulations is $512 \, \text{Mpc} \, \text{h}^{-1}$, encompassing 1024^3 particles of cold dark matter. The pixel size is 0.4 arcmin.

In these simulations, the values of the cosmological parameters fluctuate within set ranges: M_ν in $[0, 0.62]$, Ω_m in $[0.18, 0.42]$, and A_s in $[1.29, 2.91] \times 10^{-9}$. Hence, we primarily focused on constraining these three cosmological parameters, which are extensively represented by the simulations. Our primary focus was on setting bounds on these three cosmological variables, which are well represented in the simulations. The effects of radiation on background expansion and the role of massive neutrinos were incorporated, with neutrinos evolving in a perturbative manner and their clustering resulting from the nonlinear evolution of dark matter.
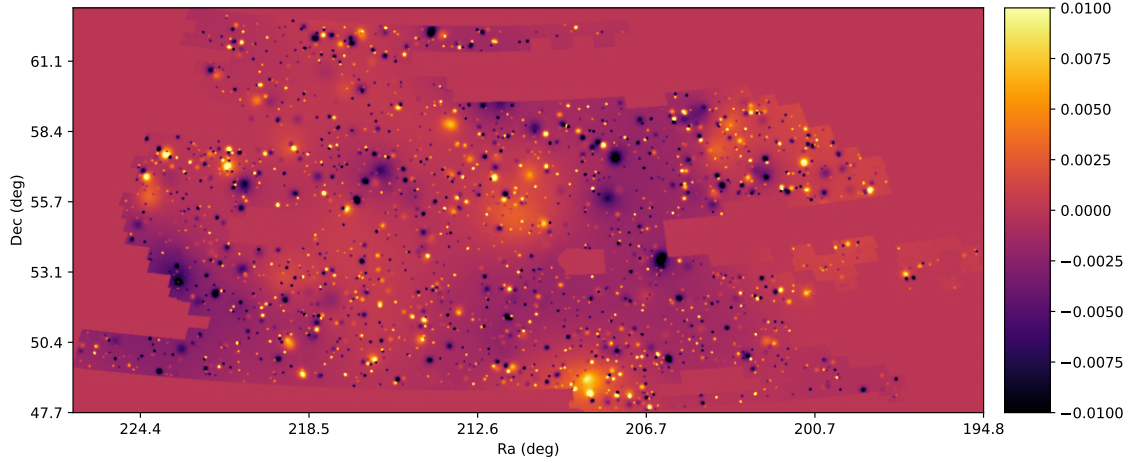
Figure 3.8: Mass map reconstructed with the sparse recovery algorithm with 20 iterations and $\lambda = 4$. The resolution is $1.5 \times 1.5 \text{ arcmin}^2$.
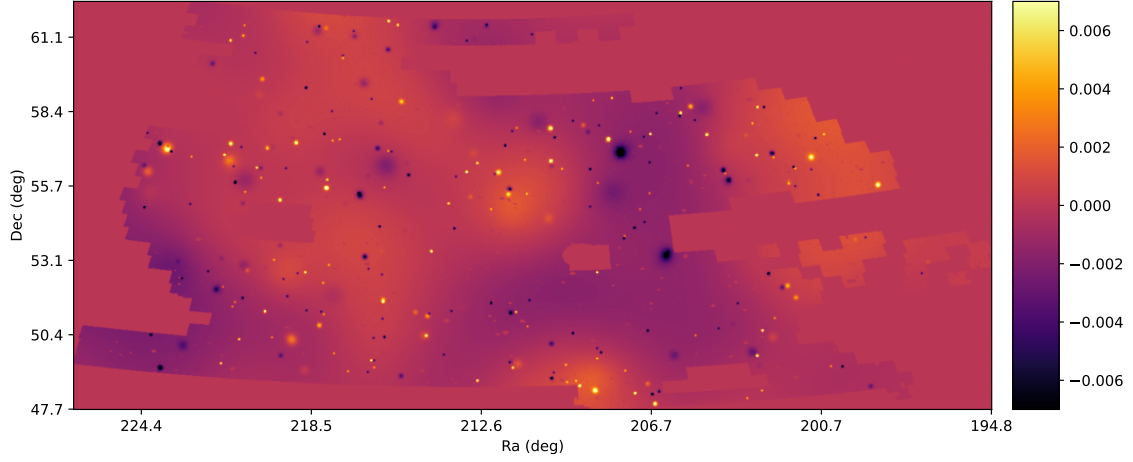

Figure 3.9: Mass map reconstructed with the sparse recovery algorithm with 20 iterations and $\lambda = 5$. The resolution is $1.5 \times 1.5 \text{ arcmin}^2$.

The simulations adopt a flat universe model with a Hubble constant $H_0 = 70 \text{km s}^{-1}\text{Mpc}^{-1}$. Additional fixed parameters include a primordial power-spectrum scalar index of $n_s = 0.97$, a baryon density of $\Omega_b = 0.046$, and a dark-energy equation of state of $w = -1$. We set a fiducial cosmology to $[M_\nu, \Omega_m, 10^9 \times A_s] = [0.1, 0.3, 2.1]$. The simulations provide data for 100 cosmologies, each offering 10000 iterations generated by random rotation and shifting of the lensing potential planes. Following [17, 20], we computed the peak counts for every cosmology from the simulated mass maps, averaged over 10000 iterations for each model. A model with massless neutrinos corresponding to $[M_\nu, \Omega_m, 10^9 \times A_s] = [0.0, 0.3, 2.1]$ was also included, and we utilized this model to compute the covariance matrix.

In order to incorporate a shape noise that reproduces the noise of the CFIS data in the simulations, we introduced Gaussian noise by calculating the overall dispersion of the ellipticity data σ_e^2 and form it computing the noise per pixel as:

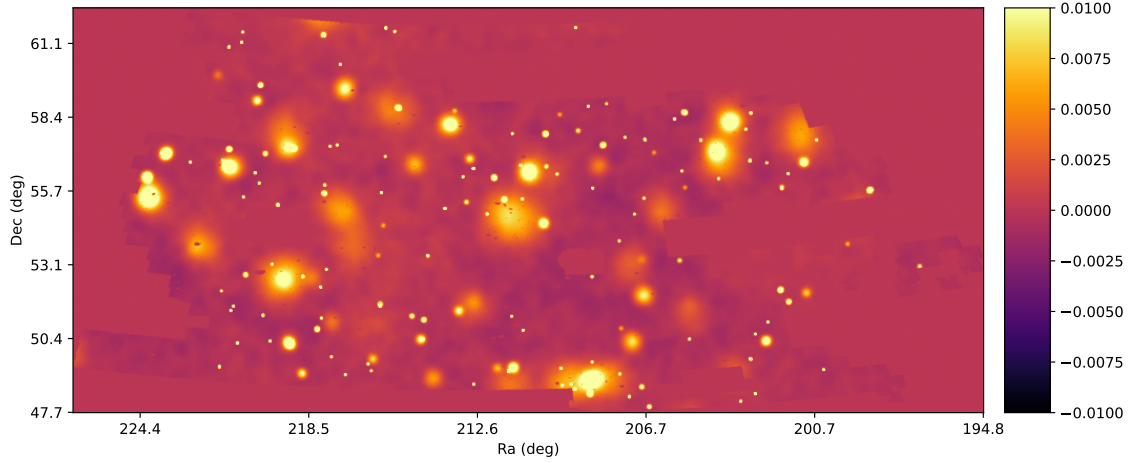$$\sigma_{\text{pix}}^2 = \frac{\sigma_e^2}{2n_{\text{gal}}A_{\text{pix}}} \tag{3.10}$$

41

Figure 3.10: Mass map reconstructed with the MCAlens algorithm with 15 iterations and $\lambda = 5$. The resolution is $1.5 \times 1.5 \text{ arcmin}^2$.

where n_{gal} is the number density of galaxies and A_{pix} is the area of a pixel. We then added this noise to the convergence maps from the simulations.

3.4.4 Cosmological inference

The result we obtained for the peak counts in the CFIS P3 patch can provide constraints on the cosmological parameters Ω_m (matter density parameter), A_s (primordial power spectrum) and M_ν (sum of neutrino masses). To do this, we implement the cosmological inference pipeline `shear-pipe-peaks` [17].

The pipeline assumes a Gaussian likelihood

$$\log \mathcal{L}(\theta) = \frac{1}{2}(d - \mu(\theta))^T C^{-1}(d - \mu(\theta)) \tag{3.11}$$

where d is the data vector, $\mu(\theta)$ is the model prediction, and C is the covariance matrix. For the model, the pipeline employs the Gaussian Process Regressor that was trained on the 100 cosmological models from the `MassiveNuS` simulations. The data vector is the peak counts in the CFIS P3 patch, using the variations of realizations from the benchmark model and thus assumed it to be independent of parameters.

The pipeline then explores the posterior distribution, using Markov-Chain-Monte-Carlo (MCMC) sampling. The sampler used in the pipeline is the `emcee` sampler with 120 walkers and 6500 steps, sweeping the parameter space around the fiducial cosmology. The cosmological parameters vary within the parameter space of the simulations across: $\Omega_m \in [0.18, 0.42]$, $A_s \in [1.29, 2.91]$, and $M_\nu \in [0.0, 0.62]$, as we described in Section 3.4.3.

The comparison of our peak counts with the predictions from the simulation results for the different cosmological models by the pipeline, generated the constraints on the cosmological parameters that can be seen in Figure 3.14. The constraints are shown as with the 68% and 95.5% confidence regions.

This result is close to the one obtained in [20]. Although it has unusual features from the cosmological point of view, our ultimate goal here was not to estimate the cosmological parameters, but rather to demonstrate the potential of the peak counts on mass maps as a cosmological probe.
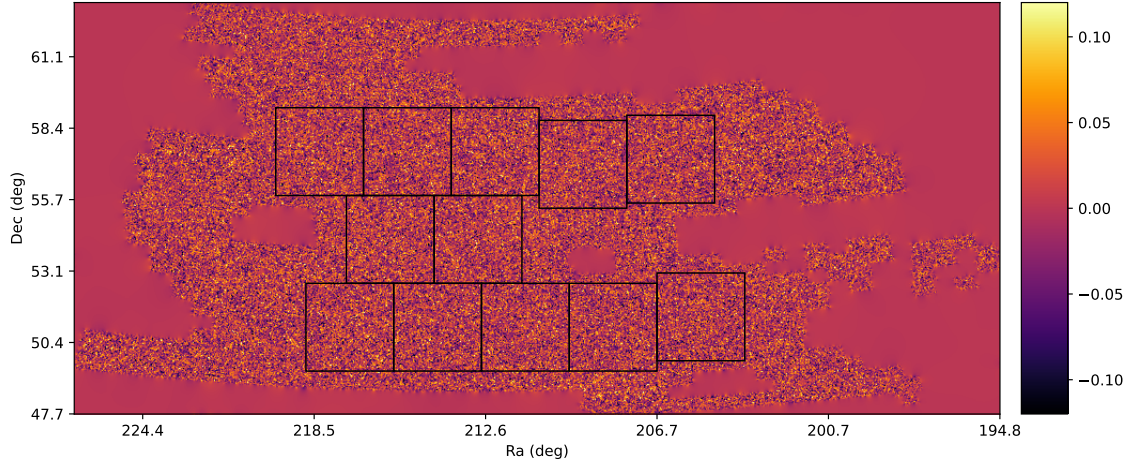
Figure 3.11: The CFIS P3 mass map with the 12 cutouts in black boxes. The cutouts are non-overlapping and away from the edges of the mass map.
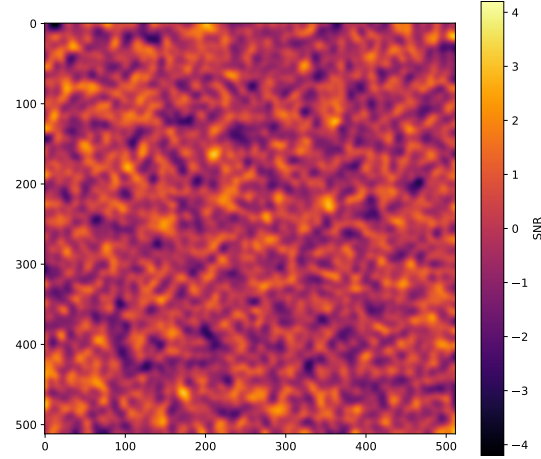

Figure 3.12: The SNR map for one of the cutouts.

The unusual features may have various sources, such as remaining biases in the data or systematics. It was shown in [20] that the final results for the constrains are sensitive to systematic effects such as local calibration, metacalibration shear bias, baryonic feedback, the source galaxy redshift estimate, intrinsic alignment, and cluster member dilution. Another possible source of the unusual features is that our catalog is small, so we expect that the constraints will improve with the full CFIS data and even more with the full UNIONS dataset.
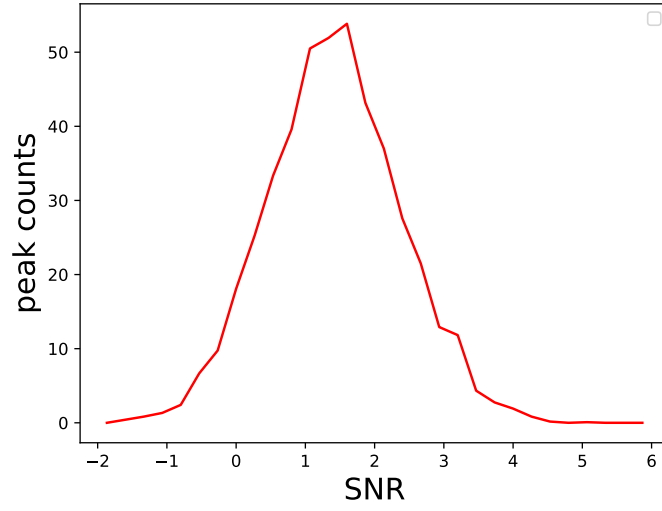
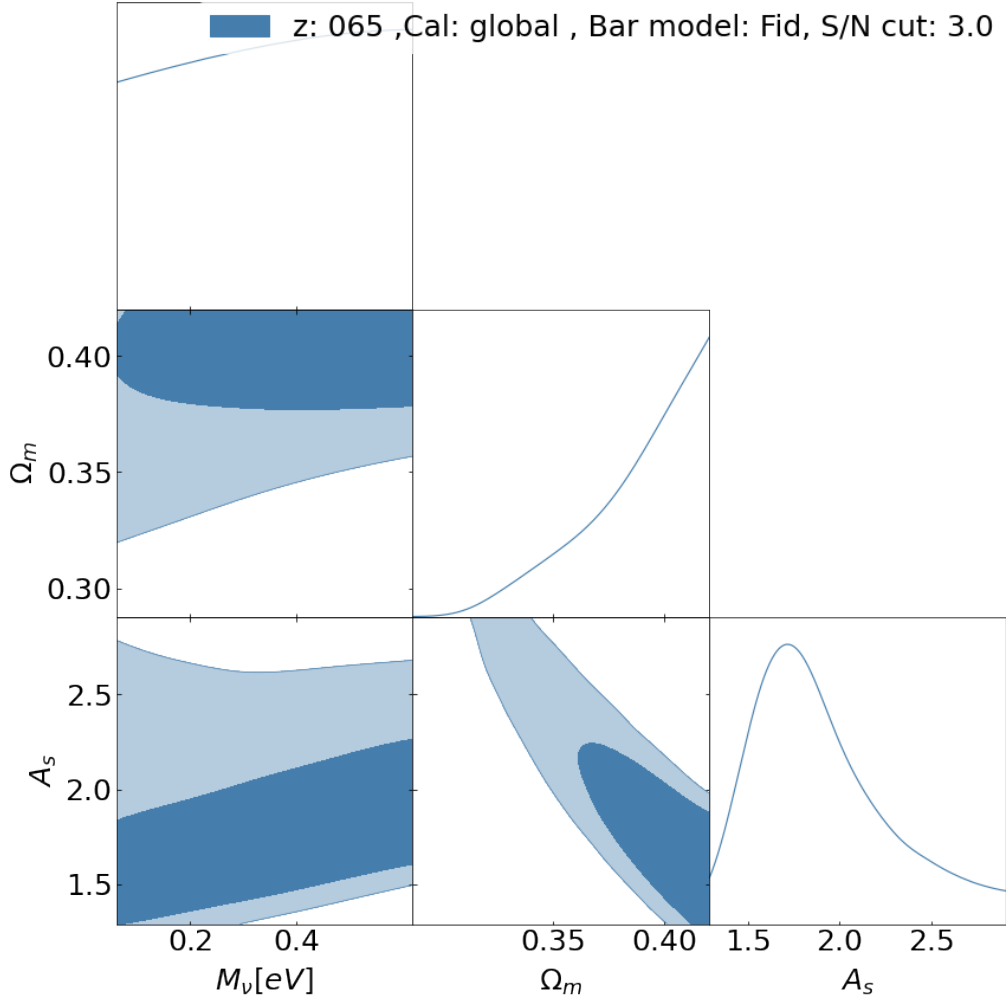Figure 3.13: The average peak counts over the 12 cutouts.

Figure 3.14: The constraints on the cosmological parameters Ω_m, A_s, and M_ν from the peak counts in the CFIS P3 patch. The 2D inner and outer contours show the 68% and 95.5% confidence regions.

Chapter 4

Conclusions, ongoing work, and future prospects

4.1 Conclusions

This work has presented a comprehensive investigation into the methods of weak gravitational lensing, focusing on the comparison and application of different mass-mapping techniques. Our study encompassed four key methods - the Kaiser-Squires technique, Wiener filter, Sparse Recovery, and MCALens, each offering unique insights into the weak lensing phenomenon and the underlying dark matter structure of the Universe.

Our comparative analysis of these techniques revealed their individual strengths and weaknesses, providing valuable context for their future applications in cosmological studies. Each method was applied to real data from the CFIS survey, leading to the generation of distinct mass maps. The comparison between the maps and their underlying techniques has shed light on the influence of the mapping method on the final result, an important factor in weak lensing studies.

Furthermore, the application of peak counting to one of the generated mass maps demonstrated how this higher-order-statistics approach can be used to probe the cosmology of the Universe. Our comparison with simulations led to constraints on cosmological parameters such as the matter density parameter (Ω_m), the primordial power spectrum (A_s), and the sum of neutrino masses (M_ν). This showcases the potential of weak lensing and specifically peak counting in probing the cosmology of our Universe.

Looking ahead, this study underscores the importance of methodological choice in weak lensing studies and the potential insights that can be gained from mass maps. As the field continues to evolve, especially with the upcoming large imaging survey by the Euclid mission, these insights will prove increasingly valuable in our pursuit to understand the nature of dark matter and the origins of the accelerated expansion of the Universe.

4.2 Ongoing work and future prospects

The work presented in this thesis is just the first step for our future research direction in weak lensing mass mapping and its utility in constraining cosmological parameters.

A part of the ongoing work involves incorporating machine learning methods such as `DeepMass`

and `DeepPosterior`, introduced in [16] and [15], respectively. Moreover, we are working on transferring our code a high-performance computing cluster, which will allow us to make mass maps of the CFIS data at the necessary resolution to conduct peak counts and carry out the cosmological inference pipeline with all of our mass mapping techniques, not just the Kaiser-Squires method used here. An important research question we aim to answer is whether different mass mapping techniques can lead to different results for the cosmological constraints. This is a contentious topic in the field, with some researchers arguing that the choice of mass mapping method does not impact the final results.

Looking beyond the scope of this thesis, there are numerous exciting prospects that we plan to explore in the near future. These include the following:

- Simulation Upgrades: An important priority is to update our simulations to Scinet Light-Cone Simulations (`SLICS`). These simulations are tailored for weak lensing studies and offer improvements over the MassiveNuS simulations used in this thesis. In particular, SLICS simulations include a number of features that better accommodate weak lensing analysis and have been utilized in the KiDS and DES surveys.

- Spherical Mass Mapping: Another direction of advancement is the transition from "flat" patch mapping to spherical mass mapping. This transition will provide a more accurate representation of the large-scale structure of the Universe. Accomplishing this will necessitate the upgrade to `CosmoGrid` simulations, which support this type of spherical analysis.

- Full Footprint Peak Counts: In the current study, peak counts were performed on a single patch of the CFIS dataset (P3). Future work will encompass peak counts across the full footprint of the survey, significantly expanding the scale of the analysis.

- Tomographic Data: We anticipate the availability of tomographic data from CFIS in the near future. This will provide the redshifts of all galaxies in the survey, allowing us to perform tomographic peak counts. The inclusion of this "time" information is vital for constraining the cosmological parameter w (dark energy equation of state), offering a deeper insight into the dynamics of our Universe.

These future developments will provide the opportunity to significantly refine our weak gravitational lensing analysis techniques, and potentially yield important insights into the fundamental nature of the Universe.

Bibliography

[1] P. Schneider, J. Ehlers, and E. E. Falco, "Gravitational lenses Springer-Verlag," *Berlin Inc., New York*, 1992.

[2] S. Seitz, P. Schneider, and J. Ehlers, "Light propagation in arbitrary spacetimes and the gravitational lens approximation," *Classical and Quantum Gravity*, vol. 11, p. 2345, June 1994.

[3] M. Bartelmann and P. Schneider, "Weak gravitational lensing," *Physics Reports*, vol. 340, pp. 291–472, Jan. 2001.

[4] M. Kilbinger, "Cosmology with cosmic shear observations: a review," *Reports on Progress in Physics*, vol. 78, p. 086901, Apr. 2015. Publisher: IOP Publishing.

[5] R. Mandelbaum, "Weak Lensing for Precision Cosmology," *Annual Review of Astronomy and Astrophysics*, vol. 56, no. 1, pp. 393–433, 2018. _eprint: https://doi.org/10.1146/annurev-astro-081817-051928.

[6] D. J. Bacon, A. R. Refregier, and R. S. Ellis, "Detection of weak gravitational lensing by large-scale structure," *Monthly Notices of the Royal Astronomical Society*, vol. 318, pp. 625–640, Oct. 2000. ADS Bibcode: 2000MNRAS.318..625B.

[7] A. Refregier, "Weak Gravitational Lensing by Large-Scale Structure," *Annual Review of Astronomy and Astrophysics*, vol. 41, no. 1, pp. 645–668, 2003. _eprint: https://doi.org/10.1146/annurev.astro.41.111302.102207.

[8] C. Shapiro and A. Cooray, "The Born and lens–lens corrections to weak gravitational lensing angular power spectra," *Journal of Cosmology and Astroparticle Physics*, vol. 2006, p. 007, Nov. 2006.

[9] V. Ajani, *Higher order statistics for cosmology : likelihood development for future surveys like Euclid*. phdthesis, Université Paris Cité, Oct. 2021.

[10] F. Bernardeau, "The effects of source clustering on weak lensing statistics," Apr. 1998. arXiv:astro-ph/9712115.

[11] P. Schneider, L. Van Waerbeke, and Y. Mellier, "B-modes in cosmic shear from source redshift clustering," *Astronomy & Astrophysics*, vol. 389, pp. 729–741, July 2002.

[12] T. Hamana, S. T. Colombi, A. Thion, J. E. G. T. Devriendt, Y. Mellier, and F. Bernardeau, "Source-lens clustering effects on the skewness of the lensing convergence," *Monthly Notices of the Royal Astronomical Society*, vol. 330, pp. 365–377, Feb. 2002.

[13] C. Seitz and P. Schneider, "Steps towards nonlinear cluster inversion through gravitational distortions: III. Including a redshift distribution of the sources," Jan. 1996. arXiv:astro-ph/9601079.

[14] N. Kaiser and G. Squires, "Mapping the Dark Matter with Weak Gravitational Lensing," *The Astrophysical Journal*, vol. 404, p. 441, Feb. 1993. ADS Bibcode: 1993ApJ...404..441K.

[15] B. Remy, F. Lanusse, N. Jeffrey, J. Liu, J.-L. Starck, K. Osato, and T. Schrabback, "Probabilistic mass-mapping with neural score estimation," *Astronomy & Astrophysics*, vol. 672, p. A51, Apr. 2023.

[16] N. Jeffrey, F. Lanusse, O. Lahav, and J.-L. Starck, "Deep learning dark matter map reconstructions from DES SV weak lensing data," *Monthly Notices of the Royal Astronomical Society*, vol. 492, no. 4, p. 5023, 2020.

[17] V. Ajani, A. Peel, V. Pettorino, J.-L. Starck, Z. Li, and J. Liu, "Constraining neutrino masses with weak-lensing multiscale peak counts," *Physical Review D*, vol. 102, p. 103531, Nov. 2020. Publisher: American Physical Society.

[18] J. Harnois-Déraps, B. Giblin, and B. Joachimi, "Cosmic shear covariance matrix in wCDM: Cosmology matters," *Astronomy & Astrophysics*, vol. 631, p. A160, Nov. 2019. Publisher: EDP Sciences.

[19] J. Harnois-Déraps, N. Martinet, T. Castro, K. Dolag, B. Giblin, C. Heymans, H. Hildebrandt, and Q. Xia, "Cosmic shear cosmology beyond two-point statistics: a combined peak count and correlation function analysis of DES-Y1," *Monthly Notices of the Royal Astronomical Society*, vol. 506, pp. 1623–1650, Sept. 2021.

[20] E. Ayçoberry, V. Ajani, A. Guinot, M. Kilbinger, V. Pettorino, S. Farrens, J.-L. Starck, R. Gavazzi, and M. J. Hudson, "UNIONS: The impact of systematic errors on weak-lensing peak counts," *Astronomy & Astrophysics*, vol. 671, p. A17, Mar. 2023. Publisher: EDP Sciences.

[21] D. Zürcher, J. Fluri, R. Sgier, T. Kacprzak, M. Gatti, C. Doux, L. Whiteway, A. Réfrégier, C. Chang, N. Jeffrey, B. Jain, P. Lemos, D. Bacon, A. Alarcon, A. Amon, K. Bechtol, M. Becker, G. Bernstein, A. Campos, R. Chen, A. Choi, C. Davis, J. Derose, S. Dodelson, F. Elsner, J. Elvin-Poole, S. Everett, A. Ferte, D. Gruen, I. Harrison, D. Huterer, M. Jarvis, P. F. Leget, N. Maccrann, J. Mccullough, J. Muir, J. Myles, A. Navarro Alsina, S. Pandey, J. Prat, M. Raveri, R. P. Rollins, A. Roodman, C. Sanchez, L. F. Secco, E. Sheldon, T. Shin, M. Troxel, I. Tutusaus, B. Yin, M. Aguena, S. Allam, F. Andrade-Oliveira, J. Annis, E. Bertin, D. Brooks, D. Burke, A. Carnero Rosell, M. Carrasco Kind, J. Carretero, F. Castander, R. Cawthon, C. Conselice, M. Costanzi, L. da Costa, M. E. da Silva Pereira, T. Davis, J. De Vicente, S. Desai, H. T. Diehl, J. Dietrich, P. Doel, K. Eckert, A. Evrard, I. Ferrero, B. Flaugher, P. Fosalba, D. Friedel, J. Frieman, J. Garcia-Bellido, E. Gaztanaga, D. Gerdes, T. Giannantonio, R. Gruendl, J. Gschwend, G. Gutierrez, S. Hinton, D. L. Hollowood, K. Honscheid, B. Hoyle, D. James, K. Kuehn, N. Kuropatkin, O. Lahav, C. Lidman, M. Lima, M. Maia, J. Marshall, P. Melchior, F. Menanteau, R. Miquel, R. Morgan, A. Palmese, F. Paz-Chinchon, A. Pieres, A. Plazas Malagón, K. Reil, M. Rodriguez Monroy, K. Romer, E. Sanchez, V. Scarpine, M. Schubnell, S. Serrano, I. Sevilla, M. Smith, E. Suchyta, G. Tarle, D. Thomas, C. To, T. N. Varga, J. Weller, R. Wilkinson, and (DES Collaboration), "Dark energy survey year 3 results: Cosmology with peaks using an emulator approach," *Monthly Notices of the Royal Astronomical Society*, vol. 511, pp. 2075–2104, Apr. 2022.

[22] T. Kacprzak, J. Fluri, A. Schneider, A. Refregier, and J. Stadel, "CosmoGridV1: a simulated wCDM theory prediction for map-level cosmological inference," *Journal of Cosmology and Astroparticle Physics*, vol. 2023, p. 050, Feb. 2023. Publisher: IOP Publishing.

[23] T. Kacprzak, D. Kirk, O. Friedrich, A. Amara, A. Refregier, L. Marian, J. P. Dietrich, E. Suchyta, J. Aleksić, D. Bacon, M. R. Becker, C. Bonnett, S. L. Bridle, C. Chang, T. F. Eifler, W. G. Hartley, E. M. Huff, E. Krause, N. MacCrann, P. Melchior, A. Nicola, S. Samuroff, E. Sheldon, M. A. Troxel, J. Weller, J. Zuntz, T. M. C. Abbott, F. B. Abdalla, R. Armstrong, A. Benoit-Lévy, G. M. Bernstein, R. A. Bernstein, E. Bertin, D. Brooks, D. L. Burke, A. C. Rosell, M. C. Kind, J. Carretero, F. J. Castander, M. Crocce, C. B. D'Andrea, L. N. da Costa, S. Desai, H. T. Diehl, A. E. Evrard, A. F. Neto, B. Flaugher, P. Fosalba, J. Frieman, D. W. Gerdes, D. A. Goldstein, D. Gruen, R. A. Gruendl, G. Gutierrez, K. Honscheid, B. Jain, D. J. James, M. Jarvis, K. Kuehn, N. Kuropatkin, O. Lahav, M. Lima, M. March, J. L. Marshall, P. Martini, C. J. Miller, R. Miquel, J. J. Mohr, R. C. Nichol, B. Nord, A. A. Plazas, A. K. Romer, A. Roodman,

E. S. Rykoff, E. Sanchez, V. Scarpine, M. Schubnell, I. Sevilla-Noarbe, R. C. Smith, M. Soares-Santos, F. Sobreira, M. E. C. Swanson, G. Tarle, D. Thomas, V. Vikram, A. R. Walker, Y. Zhang, and (The DES Collaboration), "Cosmology constraints from shear peak statistics in Dark Energy Survey Science Verification data," *Monthly Notices of the Royal Astronomical Society*, vol. 463, pp. 3653–3673, Dec. 2016.

[24] N. Jeffrey, M. Gatti, C. Chang, L. Whiteway, U. Demirbozan, A. Kovacs, G. Pollina, D. Bacon, N. Hamaus, T. Kacprzak, O. Lahav, F. Lanusse, B. Mawdsley, S. Nadathur, J. L. Starck, P. Vielzeuf, D. Zeurcher, A. Alarcon, A. Amon, K. Bechtol, G. M. Bernstein, A. Campos, A. C. Rosell, M. C. Kind, R. Cawthon, R. Chen, A. Choi, J. Cordero, C. Davis, J. DeRose, C. Doux, A. Drlica-Wagner, K. Eckert, F. Elsner, J. Elvin-Poole, S. Everett, A. Ferté, G. Giannini, D. Gruen, R. A. Gruendl, I. Harrison, W. G. Hartley, K. Herner, E. M. Huff, D. Huterer, N. Kuropatkin, M. Jarvis, P. F. Leget, N. MacCrann, J. McCullough, J. Muir, J. Myles, A. Navarro-Alsina, S. Pandey, J. Prat, M. Raveri, R. P. Rollins, A. J. Ross, E. S. Rykoff, C. Sánchez, L. F. Secco, I. Sevilla-Noarbe, E. Sheldon, T. Shin, M. A. Troxel, I. Tutusaus, T. N. Varga, B. Y. B. Yin, Y. Zhang, J. Zuntz, T. M. C. Abbott, M. Aguena, S. Allam, F. Andrade-Oliveira, M. R. Becker, E. Bertin, S. Bhargava, D. Brooks, D. L. Burke, J. Carretero, F. J. Castander, C. Conselice, M. Costanzi, M. Crocce, L. N. da Costa, M. E. S. Pereira, J. De Vicente, S. Desai, H. T. Diehl, J. P. Dietrich, P. Doel, I. Ferrero, B. Flaugher, P. Fosalba, J. García-Bellido, E. Gaztanaga, D. W. Gerdes, T. Giannantonio, J. Gschwend, G. Gutierrez, S. R. Hinton, D. L. Hollowood, B. Hoyle, B. Jain, D. J. James, M. Lima, M. A. G. Maia, M. March, J. L. Marshall, P. Melchior, F. Menanteau, R. Miquel, J. J. Mohr, R. Morgan, R. L. C. Ogando, A. Palmese, F. Paz-Chinchón, A. A. Plazas, M. Rodriguez-Monroy, A. Roodman, E. Sanchez, V. Scarpine, S. Serrano, M. Smith, M. Soares-Santos, E. Suchyta, G. Tarle, D. Thomas, C. To, and J. Weller, "Dark Energy Survey Year 3 results: curved-sky weak lensing mass map reconstruction," *Monthly Notices of the Royal Astronomical Society*, vol. 505, pp. 4626–4645, June 2021. arXiv:2105.13539 [astro-ph].

[25] M. Bartelmann, "Cluster mass estimates from weak lensing," Dec. 1994. arXiv:astro-ph/9412051.

[26] N. Kaiser, "Nonlinear Cluster Lens Reconstruction," *The Astrophysical Journal*, vol. 439, p. L1, Jan. 1995. ADS Bibcode: 1995ApJ...439L...1K.

[27] G. Squires and N. Kaiser, "Unbiased Cluster Lens Reconstruction," *The Astrophysical Journal*, vol. 473, p. 65, Dec. 1996.

[28] J.-L. Starck, S. Pires, and A. Réfrégier, "Weak lensing mass reconstruction using wavelets," *Astronomy & Astrophysics*, vol. 451, pp. 1139–1150, June 2006.

[29] N. Jeffrey, M. Gatti, C. Chang, L. Whiteway, U. Demirbozan, A. Kovacs, G. Pollina, D. Bacon, N. Hamaus, T. Kacprzak, O. Lahav, F. Lanusse, B. Mawdsley, S. Nadathur, J. L. Starck, P. Vielzeuf, D. Zeurcher, A. Alarcon, A. Amon, K. Bechtol, G. M. Bernstein, A. Campos, A. C. Rosell, M. C. Kind, R. Cawthon, R. Chen, A. Choi, J. Cordero, C. Davis, J. DeRose, C. Doux, A. Drlica-Wagner, K. Eckert, F. Elsner, J. Elvin-Poole, S. Everett, A. Ferté, G. Giannini, D. Gruen, R. A. Gruendl, I. Harrison, W. G. Hartley, K. Herner, E. M. Huff, D. Huterer, N. Kuropatkin, M. Jarvis, P. F. Leget, N. MacCrann, J. McCullough, J. Muir, J. Myles, A. Navarro-Alsina, S. Pandey, J. Prat, M. Raveri, R. P. Rollins, A. J. Ross, E. S. Rykoff, C. Sánchez, L. F. Secco, I. Sevilla-Noarbe, E. Sheldon, T. Shin, M. A. Troxel, I. Tutusaus, T. N. Varga, B. Y. B. Yin, Y. Zhang, J. Zuntz, T. M. C. Abbott, M. Aguena, S. Allam, F. Andrade-Oliveira, M. R. Becker, E. Bertin, S. Bhargava, D. Brooks, D. L. Burke, J. Carretero, F. J. Castander, C. Conselice, M. Costanzi, M. Crocce, L. N. da Costa, M. E. S. Pereira, J. De Vicente, S. Desai, H. T. Diehl, J. P. Dietrich, P. Doel, I. Ferrero, B. Flaugher, P. Fosalba, J. García-Bellido, E. Gaztanaga, D. W. Gerdes, T. Giannantonio, J. Gschwend, G. Gutierrez, S. R. Hinton, D. L. Hollowood, B. Hoyle, B. Jain, D. J. James, M. Lima, M. A. G. Maia, M. March, J. L. Marshall, P. Melchior, F. Menanteau, R. Miquel, J. J. Mohr, R. Morgan, R. L. C. Ogando, A. Palmese, F. Paz-Chinchón, A. A. Plazas, M. Rodriguez-Monroy, A. Roodman, E. Sanchez, V. Scarpine, S. Serrano, M. Smith, M. Soares-Santos, E. Suchyta, G. Tarle, D. Thomas, C. To,

and J. Weller, "Dark Energy Survey Year 3 results: curved-sky weak lensing mass map reconstruction," *Monthly Notices of the Royal Astronomical Society*, vol. 505, pp. 4626–4645, June 2021. arXiv:2105.13539 [astro-ph].

[30] J.-L. Starck, K. E. Themelis, N. Jeffrey, A. Peel, and F. Lanusse, "Weak-lensing mass reconstruction using sparsity and a Gaussian random field," *Astronomy & Astrophysics*, vol. 649, p. A99, May 2021.

[31] N. Jeffrey, F. B. Abdalla, O. Lahav, F. Lanusse, J.-L. Starck, A. Leonard, D. Kirk, C. Chang, E. Baxter, T. Kacprzak, S. Seitz, V. Vikram, L. Whiteway, T. M. C. Abbott, S. Allam, S. Avila, E. Bertin, D. Brooks, A. Carnero Rosell, M. Carrasco Kind, J. Carretero, F. J. Castander, M. Crocce, C. E. Cunha, C. B. D'Andrea, L. N. da Costa, C. Davis, J. De Vicente, S. Desai, P. Doel, T. F. Eifler, A. E. Evrard, B. Flaugher, P. Fosalba, J. Frieman, J. García-Bellido, D. W. Gerdes, D. Gruen, R. A. Gruendl, J. Gschwend, G. Gutierrez, W. G. Hartley, K. Honscheid, B. Hoyle, D. J. James, M. Jarvis, K. Kuehn, M. Lima, H. Lin, M. March, P. Melchior, F. Menanteau, R. Miquel, A. A. Plazas, K. Reil, A. Roodman, E. Sanchez, V. Scarpine, M. Schubnell, I. Sevilla-Noarbe, M. Smith, M. Soares-Santos, F. Sobreira, E. Suchyta, M. E. C. Swanson, G. Tarle, D. Thomas, A. R. Walker, and DES Collaboration, "Improving weak lensing mass map reconstructions using Gaussian and sparsity priors: application to DES SV," *Monthly Notices of the Royal Astronomical Society*, vol. 479, pp. 2871–2888, Sept. 2018.

[32] E. Ayçoberry, V. Ajani, A. Guinot, M. Kilbinger, V. Pettorino, S. Farrens, J.-L. Starck, R. Gavazzi, and M. J. Hudson, "UNIONS: The impact of systematic errors on weak-lensing peak counts," *Astronomy & Astrophysics*, vol. 671, p. A17, Mar. 2023. arXiv:2204.06280 [astro-ph].

[33] A. Peel, C.-A. Lin, F. Lanusse, A. Leonard, J.-L. Starck, and M. Kilbinger, "Cosmological constraints with weak-lensing peak counts and second-order statistics in a large-field survey," *Astronomy & Astrophysics*, vol. 599, p. A79, Mar. 2017.

[34] A. Guinot, M. Kilbinger, S. Farrens, A. Peel, A. Pujol, M. Schmitz, J.-L. Starck, T. Erben, R. Gavazzi, S. Gwyn, M. J. Hudson, H. Hildebrandt, L. Tobias, L. Miller, I. Spitzer, L. Van Waerbeke, J.-C. Cuillandre, S. Fabbro, A. McConnachie, and Y. Mellier, "ShapePipe: A new shape measurement pipeline and weak-lensing application to UNIONS/CFIS data," *Astronomy & Astrophysics*, vol. 666, p. A162, Oct. 2022.

[35] H. Shan, J.-P. Kneib, J. Comparat, E. Jullo, A. Charbonnier, T. Erben, M. Makler, B. Moraes, L. Van Waerbeke, F. Courbin, G. Meylan, C. Tao, and J. E. Taylor, "Weak lensing mass map and peak statistics in Canada–France–Hawaii Telescope Stripe 82 survey," *Monthly Notices of the Royal Astronomical Society*, vol. 442, pp. 2534–2542, Aug. 2014.

[36] M. Gatti, B. Jain, C. Chang, M. Raveri, D. Zürcher, L. Secco, L. Whiteway, N. Jeffrey, C. Doux, T. Kacprzak, D. Bacon, P. Fosalba, A. Alarcon, A. Amon, K. Bechtol, M. Becker, G. Bernstein, J. Blazek, A. Campos, A. Choi, C. Davis, J. Derose, S. Dodelson, F. Elsner, J. Elvin-Poole, S. Everett, A. Ferte, D. Gruen, I. Harrison, D. Huterer, M. Jarvis, E. Krause, P. Leget, P. Lemos, N. Maccrann, J. Mccullough, J. Muir, J. Myles, A. Navarro, S. Pandey, J. Prat, R. Rollins, A. Roodman, C. Sanchez, E. Sheldon, T. Shin, M. Troxel, I. Tutusaus, B. Yin, M. Aguena, S. Allam, F. Andrade-Oliveira, J. Annis, E. Bertin, D. Brooks, D. Burke, A. Carnero Rosell, M. Carrasco Kind, J. Carretero, R. Cawthon, M. Costanzi, L. Da Costa, M. Pereira, J. De Vicente, S. Desai, H. Diehl, J. Dietrich, P. Doel, A. Drlica-Wagner, K. Eckert, A. Evrard, I. Ferrero, J. García-Bellido, E. Gaztanaga, T. Giannantonio, R. Gruendl, J. Gschwend, G. Gutierrez, S. Hinton, D. Hollowood, K. Honscheid, D. James, K. Kuehn, N. Kuropatkin, O. Lahav, C. Lidman, M. Maia, J. Marshall, P. Melchior, F. Menanteau, R. Miquel, R. Morgan, A. Palmese, F. Paz-Chinchón, A. Pieres, A. Plazas Malagón, K. Reil, M. Rodriguez-Monroyv, A. Romer, E. Sanchez, M. Schubnell, S. Serrano, I. Sevilla-Noarbe, M. Smith, M. Soares-Santos, E. Suchyta, G. Tarle, D. Thomas, C. To, T. Varga, and DES Collaboration, "Dark Energy Survey Year 3 results: Cosmology with moments of weak lensing mass maps," *Physical Review D*, vol. 106, p. 083509, Oct. 2022.

[37] F. Lanusse, J.-L. Starck, A. Leonard, and S. Pires, "High resolution weak lensing mass mapping combining shear and flexion," *Astronomy & Astrophysics*, vol. 591, p. A2, July 2016. Publisher: EDP Sciences.

[38] D. N. Limber, "The Analysis of Counts of the Extragalactic Nebulae in Terms of a Fluctuating Density Field.," *The Astrophysical Journal*, vol. 117, p. 134, Jan. 1953. ADS Bibcode: 1953ApJ...117..134L.

[39] N. Kaiser, "Weak Gravitational Lensing of Distant Galaxies," *The Astrophysical Journal*, vol. 388, p. 272, Apr. 1992. ADS Bibcode: 1992ApJ...388..272K.

[40] P. Simon, "How accurate is Limber's equation?," *Astronomy & Astrophysics*, vol. 473, pp. 711–714, Oct. 2007. Number: 3 Publisher: EDP Sciences.

[41] P. Lemos, A. Challinor, and G. Efstathiou, "The effect of Limber and flat-sky approximations on galaxy weak lensing," *Journal of Cosmology and Astroparticle Physics*, vol. 2017, p. 014, May 2017.

[42] N. Wiener, "Extrapolation, Interpolation, and Smoothing of Stationary Time Series, with Engineering Applications,"

[43] F. Elsner and B. D. Wandelt, "Efficient Wiener filtering without preconditioning," *Astronomy & Astrophysics*, vol. 549, p. A111, Jan. 2013.

[44] J. Bobin, J.-L. Starck, F. Sureau, and J. Fadili, "CMB Map Restoration," *Advances in Astronomy*, vol. 2012, pp. 1–15, 2012.

[45] D. K. Ramanah, G. Lavaux, and B. D. Wandelt, "Wiener filtering and pure E/B decomposition of CMB maps with anisotropic correlated noise," *Monthly Notices of the Royal Astronomical Society*, vol. 490, pp. 947–961, Nov. 2019. arXiv:1906.10704 [astro-ph].

[46] J. L. Starck, E. Pantin, and F. Murtagh, "Deconvolution in Astronomy: A Review," *Publications of the Astronomical Society of the Pacific*, vol. 114, p. 1051, Oct. 2002. Publisher: IOP Publishing.

[47] J.-L. Starck, S. Pires, and A. Réfrégier, "Weak lensing mass reconstruction using wavelets," *Astronomy & Astrophysics*, vol. 451, pp. 1139–1150, June 2006.

[48] A. Guinot, *Weak lensing analysis of the Canada-France Imaging Survey : from pixels to cosmology, preparation for the Euclid mission*. These de doctorat, Université Paris Cité, Dec. 2020.

[49] A. Guinot, M. Kilbinger, S. Farrens, A. Peel, A. Pujol, M. Schmitz, J.-L. Starck, T. Erben, R. Gavazzi, S. Gwyn, M. J. Hudson, H. Hiledebrandt, T. Liaudat, L. Miller, I. Spitzer, L. Van Waerbeke, J.-C. Cuillandre, S. Fabbro, and A. McConnachie, "ShapePipe: a new shape measurement pipeline and weak-lensing application to UNIONS/CFIS data," *Astronomy & Astrophysics*, vol. 666, p. A162, Oct. 2022. arXiv:2204.04798 [astro-ph].

[50] C. Heymans, L. Van Waerbeke, L. Miller, T. Erben, H. Hildebrandt, H. Hoekstra, T. D. Kitching, Y. Mellier, P. Simon, C. Bonnett, J. Coupon, L. Fu, J. Harnois Déraps, M. J. Hudson, M. Kilbinger, K. Kuijken, B. Rowe, T. Schrabback, E. Semboloni, E. van Uitert, S. Vafaei, and M. Velander, "CFHTLenS: the Canada-France-Hawaii Telescope Lensing Survey," *Monthly Notices of the Royal Astronomical Society*, vol. 427, pp. 146–166, Nov. 2012. ADS Bibcode: 2012MNRAS.427..146H.

[51] E. Huff and R. Mandelbaum, "Metacalibration: Direct Self-Calibration of Biases in Shear Measurement," Feb. 2017. arXiv:1702.02600 [astro-ph].

[52] P. Fosalba, M. Crocce, E. Gaztañaga, and F. J. Castander, "The MICE grand challenge lightcone simulation – I. Dark matter clustering," *Monthly Notices of the Royal Astronomical Society*, vol. 448, pp. 2987–3000, Apr. 2015.

[53] M. Elad, J. L. Starck, P. Querre, and D. L. Donoho, "Simultaneous cartoon and texture image inpainting using morphological component analysis (MCA)," *Applied and Computational Harmonic Analysis*, vol. 19, pp. 340–358, Nov. 2005.

[54] J.-L. Starck, D. Donoho, and M. Elad, "Redundant multiscale transforms and their application for morphological component separation," tech. rep., CM-P00052061, 2004.